Sedimentology, chemostratigraphy, and stromatolites of lower Paleoproterozoic carbonates, Turee Creek Group, Western Australia

Sedimentology, chemostratigraphy, and stromatolites of lower Paleoproterozoic carbonates, Turee Creek Group, Western Australia

Rowan C. Martindale [a, b, *], Justin V. Strauss [c], Erik A. Sperling [c], Jena E. Johnson [d], Martin J. Van Kranendonk [e], David Flannery [f, g], Katherine French [h], Kevin Lepot [i], Rajat Mazumder [j], Melissa S. Rice [d, k], Daniel P. Schrag [c], Roger Summons [h], Malcolm Walter [f], John Abelson [l], Andrew H. Knoll [a, c]

[a] Department of Organismic and Evolutionary Biology, Harvard University, 26 Oxford Street, Cambridge, Massachusetts, USA, 02138

[b] Department of Geological Sciences, University of Texas at Austin, 1 University Station C1100, Austin, Texas, USA, 78712

[c] Department of Earth and Planetary Sciences, Harvard University, 20 Oxford Street, Cambridge, Massachusetts, USA 02138

[d] Division of Geological and Planetary Sciences, California Institute of Technology, 1200 E California Blvd, Pasadena CA 91125

[e] Australian Centre for Astrobiology and School of Biological Earth and Environmental Sciences, University of New South Wales Australia, Kensington, NSW 2052 Australia

[f] Australian Centre for Astrobiology and School of Biotechnology and Biomolecular Sciences, University of New South Wales Australia, Kensington, NSW 2052 Australia

[g] Jet Propulsion Laboratory, California Institute of Technology, 1200 E California Blvd, Pasadena CA 91125

[h] Department of Earth, Atmospheric, and Planetary Sciences; Massachusetts Institute of Technology, Cambridge, MA 02139, USA.

[i] Laboratoire d'Océanologie et de Géosciences, Université de Lille, CNRS UMR8187, 59655 Villeneuve d'Ascq, France.

[j] Department of Applied Geology, Faculty of Engineering and Science, Curtin University Sarawak, CDT 250, 98009 Miri, Sarawak, Malaysia.

[k] Melissa S. Rice, Geology Department, Western Washington University, 516 High Street, MS 9080, Bellingham, WA 98225

[l] The Agouron Institute, Pasadena, CA 91106, USA

*Corresponding author

e-mail address: Martindale@jsg.utexas.edu

Telephone Number: 1–512-475-6439

Address: 1 University Station C1100

Austin, TX, USA, 78712

ABSTRACT

The ca. 2.45–2.22 Ga Turee Creek Group, Western Australia, contains carbonate-rich horizons that postdate earliest Proterozoic iron formations, bracket both Paleoproterozoic glaciogenic beds and the onset of the Great Oxidation Event (GOE), and predate ca. 2.2–2.05 Ga Lomagundi-Jatuli C-isotopic excursion(s). As such, Turee Creek carbonate strata provide an opportunity to characterize early Paleoproterozoic carbonate sedimentation and carbon cycle dynamics in the context of significant global change. Here, we report on the stratigraphy, sedimentology, petrology, carbon isotope chemostratigraphy, and stromatolite development for carbonate-rich successions within the pre-glacial part of the Kungarra Formation and the postglacial Kazput Formation.

Kungarra carbonate units largely occur as laterally discontinuous beds within a thick, predominantly siliciclastic shelf deposit. While this succession contains thin microbialite horizons, most carbonates consist of patchy calcite overgrowths within a siliciclastic matrix. C-isotopic values show marked variation along a single horizon and even within hand samples, reflecting spatially and temporally variable mixing between dissolved inorganic carbon in seawater and isotopically light inorganic carbon generated via syn- and post-depositional remineralization of organic matter.

In contrast, the Kazput carbonates consist of subtidal stromatolites, grainstones, and micrites deposited on a mixed carbonate-siliciclastic shelf. These carbonates exhibit moderate $\delta^{13}C$ values of -2‰ to +1.5‰ and likely preserve a C-isotopic signature of seawater. Kazput carbonates, thus, provide some of the best available evidence that an interval of unexceptional C-isotopic values separates the Lomagundi-Jatuli C-isotopic excursion(s) from the initiation of the GOE as inferred from multiple sulfur isotopes (loss

of mass independent fractionation). The Kazput Formation also contains unusual, m-scale stromatolitic buildups, which are composed of sub-mm laminae and discontinuous, convex upward lenticular precipitates up to a few mm in maximum thickness. Laminae, interpreted as microbial mat layers, contain quartz and clay minerals as well as calcite, whereas precipitate lenses consist of interlocking calcite anhedra, sometimes showing faint mm-scale banding. These cements formed either as infillings of primary voids formed by gas emission within penecontemporaneously lithified mats, or as local seafloor precipitates that formed on, or within, surface mats. It is possible that both mechanisms interacted to form the unique Kazput stromatolites. These microbialites speak to a distinctive interaction between life and environment early in the Paleoproterozoic Era.

Keywords: Turee Creek Group; Kazput Formation; Kungarra Formation; Great Oxidation Event; stromatolite; Lomagundi-Jatuli Event.

1. Introduction

Lower Paleoproterozoic sedimentary rocks record a number of first-order changes in the Earth system, including globally extensive ice sheets, one or more extreme states of the carbon cycle characterized by uniquely high $\delta^{13}C$ in carbonates, and the initial accumulation of oxygen in the atmosphere and surface oceans (Akin et al., 2013; Asael et al., 2013; Bekker and Holland, 2012; Bekker et al., 2004, 2013; Farquhar et al., 2000; Fralick et al., 2011; Hoffman, 2013; Konhauser et al., 2011; Lyons et al., 2012, 2014; Melezhik and Fallick, 2010; Partin et al., 2013; Planavsky et al., 2012, 2014; Pufahl and Hiatt, 2012; Pufahl et al., 2010, 2011; Reinhard et al., 2013; Scott et al., 2014; Swanner et

al., 2014; and references therein). Co-occurring global glaciation, carbon isotopic variation, and redox change also characterize Neoproterozoic rocks, and for this younger interval, carbonate strata have played an important role in both recording key events and providing context for the interpretation of these events (e.g., Halverson and Shields-Zhou, 2011; Johnston et al., 2012). Detailed analyses of platform and shelf carbonates are available for Neoarchean successions [e.g., the Campbellrand/Malmani subgroups of the Transvaal Supergroup, South Africa; (Knoll and Beukes, 2009; and references therein)] and younger Paleoproterozoic rocks [e.g., 2 Ga platform carbonates of the Slave Province, Canada; (Hotinski et al., 2004)]. To date, however, relatively few studies have focused on lower Paleoproterozoic carbonates, despite their potential importance in understanding early Paleoproterozoic evolution and environmental change.

The ca. 2.45–2.22 Ga Turee Creek Group, exposed in the Hamersley Range of Western Australia, conformably overlies earliest Paleoproterozoic iron formations, predates the ca. 2.2 Ga onset of the Lomagundi-Jatuli C-isotopic excursion(s), and hosts carbonate and glacially-influenced strata that record onset of the Great Oxidation Event (GOE) (Bekker et al., 2004; Martin et al., 2013; Van Kranendonk and Mazumder, 2015). Thus, these carbonates provide an opportunity to characterize the response of early Paleoproterozoic carbonate deposition and carbon cycle dynamics to significant global change, including the GOE and glaciation. Here, we report on the stratigraphy, sedimentology, carbonate petrology, carbon isotope chemostratigraphy, and stromatolite development in two closely spaced sections of the Kazput Formation of the upper Turee Creek Group. We also report lithological and isotopic data from three parallel stratigraphic sections from the older Kungarra Formation of the lower Turee Creek

Group. Together, these data place carbonate strata of the Turee Creek Group in the context of profound global change following the early oxygenation of Earth's surface environments.

2. Geologic Setting

The Turee Creek Group of the Mount Bruce Supergroup is the youngest sedimentary succession within the Hamersley Basin of the Pilbara Craton (Trendall, 1990). Turee Creek Group rocks conformably overlie iron formations of the Hamersley Group and sit unconformably beneath sedimentary and volcanic deposits of the Wyloo Group (Fig. 1) (Horwitz, 1982; Thorne, 1990; Thorne and Seymour, 1991; Trendall, 1969; Trendall et al., 1983). Initial research suggested conformable relationships throughout the Proterozoic stratigraphy of Western Australia (e.g., Trendall and Blockley, 1970), but continuing stratigraphic and geochronological studies have since identified significant unconformities and deformational events that point to a protracted, but episodic, depositional history spanning more than 330 Myr (Martin et al., 2000; and references therein).

Palinspastic reconstructions and basin analysis of upper Hamersley Basin and lower Wyloo Group stratigraphy led Horwitz (1982) to propose a post-Hamersley depositional feature, called the McGrath Trough, that reflects flexural subsidence driven by peripheral or retroarc foreland basin development (Horwitz, 1982; Krapež, 1996; Martin, 1999; Martin et al., 2000; Powell and Horwitz, 1994). The foreland-related tectonostratigraphic sequence most likely involves the Turee Creek and lower Wyloo groups (Martin et al., 2000); however, some authors have argued that it only involves the

Turee Creek Group (e.g., Blake and Barley, 1992; Krapež, 1996) or both the Turee Creek and entire Wyloo groups (e.g., Thorne and Seymour, 1991; Tyler and Thorne, 1990). More recently, Van Kranendonk et al. (2015) suggested the Turee Creek Group was deposited in an intracratonic basin. Regardless of McGrath dynamics, the 3–4 km thick Turee Creek Group records rapid lateral facies change (e.g., Martin et al., 2000 and references therein).

The Turee Creek Group consists, in stratigraphic order, of the Kungarra (including the glaciogenic Meteorite Bore Member), Koolbye, and Kazput formations (Fig. 1) (Thorne et al., 1995; Trendall, 1979, 1981). It is bracketed in age by the 2449 ± 3 Ma Woongarra Rhyolite (Barley et al., 1997) near the top of the underlying Hamersley Group and the 2209 ± 15 Ma Cheela Springs Basalt (Martin et al., 1998) low in the unconformably overlying Wyloo Group succession (Fig. 1). Müller et al. (2005) reinterpreted the Cheela Springs date as a reflection of provenance rather than crystallization age, but their U-Pb age on baddeleyite of 2208 ± 15 Ma for diorite sills that cut the Turee Creek Group provides an essentially indistinguishable maximum age constraint. The Kungarra Formation of the Turee Creek Group is further constrained to be younger than ca. 2420 Ma, based on U-Pb ages of detrital zircons in the Meteorite Bore Member (Takehara et al., 2010). Turee Creek Group strata record a broad shallowing-upward profile from deep-water banded iron formation (the Boolgeeda Iron Formation of the underlying Hamersley Group), through fine-grained siliciclastic deposits of the Kungarra Formation, to fluvial and shallow marine strata of the Koolbye and Kazput formations.

153 Although detailed correlation with other Paleoproterozoic successions is
154 challenging, Turee Creek Group strata record two events that guide interbasinal
155 correlation. First, Williford et al. (2011) documented mass independent sulfur isotope
156 fractionation, a proxy for the near-absence of environmental oxygen (Farquhar et al.,
157 2000), in the lower part of the Meteorite Bore Member of the Kungarra Formation. On
158 this basis, the authors suggested that the lower glaciogenic unit of the Meteorite Bore
159 Member, locally in contact with the Boolgeeda Iron Formation, was deposited during the
160 final stages of the GOE, when oxygen levels were still low enough for the development
161 of MIF-S, but sufficiently high for oxidative weathering of continental sulfides and
162 significant sulfur isotope fractionation.
163 The glacial character of the Meteorite Bore Member and a second recently
164 discovered unit of glacial diamictite in the Kungarra Formation provide a means of
165 correlation to other Paleoproterozoic basins (Martin, 1999; Trendall, 1976; Van
166 Kranendonk and Mazumder, 2015). Martin (1999) and Van Kranendonk et al. (2012)
167 pointed to analogous basin histories of the South African Transvaal Supergroup and the
168 Canadian Huronian Supergroup on the basis of similar ca. 2.45 Ga felsic magmatic
169 events followed by glacial episodes and mafic magmatism at ca. 2.2 Ga. Hoffman (2013)
170 suggested a similar global correlation scheme based on the assumption that the GOE, as
171 marked by the disappearance of MIF-S, was a unique event connected in time to a
172 Snowball Earth event (Kirschvink et al., 2000). By this reasoning, disparate sedimentary
173 rocks may be correlated by a single tie point, even though some regions record three
174 glacial events and others only record two. Thus, while it is difficult to assign an exact age
175 to the Turee Creek Group, the glacial history of these strata generally enables broad

176 correlation to the timing of the Great Oxidation Event (Van Kranendonk and Mazumder,
177 2015).
178
179 **3. Methods**
180 Fieldwork for this project was conducted as part of the 2012 Advanced
181 Geobiology Course sponsored by the Agouron Institute. Five stratigraphic sections were
182 measured and sampled from three sites in the Hardey Syncline: the Horseshoe Creek
183 locality of Lindsay and Brasier (2002) (Fig. 1, three sections at site 1) and two Kazput
184 Formation localities, K1 and K2, on the southwest and northeast limbs of a small NNW-
185 SSE-trending anticline in the central part of the Syncline (Fig. 1, sites 2 and 3). The
186 Horseshoe Creek strata were previously described by Lindsay and Brasier (2002) as
187 Kazput Formation, but regional mapping places this section below the Meteorite Bore
188 Member and is thus part of the Kungarra Formation (Fig. 1) (Martin et al., 2000; Van
189 Kranendonk, 2010; Van Kranendonk et al., 2015).
190 At Horseshoe Creek, three parallel stratigraphic columns were measured through
191 ~120 m of the Kungarra Formation to determine patterns of lateral facies change and
192 geochemical variation (HC1, HC2, and HC3). The first Kazput section was measured
193 through roughly 140 m of sedimentary rocks on the west-southwestern limb of the
194 anticline (locality K1), and the second section is a composite stratigraphic column
195 measured across two ridges (roughly 100 m apart) on the southwestern limb of the
196 anticline (localities K2A, K2B, and K2C). Although the K1 and K2 localities are within a
197 few kilometers of each other, their exact correlation is uncertain due to differing facies
198 development and structural complications.

199 Rock samples were collected from each measured section at roughly 1–3 m
200 intervals for geochemical and petrological analysis; samples were cut using a diamond
201 saw, and made into thin sections for petrographic analysis. Thin section blanks were then
202 microdrilled following methods of Kaufman et al. (1990) to obtain fresh powder. Blanks
203 were commonly drilled several times if multiple lithologies or microfacies were present
204 in a single thin section.
205 Carbonate $\delta^{13}C$ and $\delta^{18}O$ values for 225 Kazput and 125 Kungarra samples were
206 measured on a VG Optima dual inlet mass spectrometer fed by an Isocarb preparation
207 device in the Harvard University Laboratory for Geochemical Oceanography (see
208 supplementary data). Approximately 1 mg of carbonate powder was dissolved in a
209 common anhydrous phosphoric acid (H_3PO_4) bath kept at 90°C for eight minutes. Carbon
210 dioxide gas was purified cryogenically and measured against an in-house reference gas.
211 No dolomite corrections were applied to the data. Analytical uncertainty was ±0.1‰
212 (sample:standard ratio of 8:1); results are reported on a Vienna Pee Dee Belemnite scale.
213 Two samples were additionally analyzed using a scanning electron microscope
214 (SEM) with an attached electron dispersive spectrometer (EDS). These small-scale
215 analyses are employed to visualize and compare textures of the two carbonates, as well as
216 to provide a high-resolution map of the stromatolitic laminae from the Kazput Formation.
217 A representative sample from the Kungarra Formation (from 16.25 m in section HC3)
218 and a stromatolite from the Kazput Formation (KAZS1), were photographed using
219 backscatter detector imaging to highlight compositional contrasts on a Zeiss 1550VP
220 Field Emission SEM in the California Institute of Technology Geological and Planetary
221 Sciences Division Analytical Facility. An Oxford INCA Energy 300 EDS system was

utilized to produce elemental color maps of key elements [Si, Ca, C, Fe, Al, Mg] and these maps were superimposed on backscatter images to highlight different minerals. Elemental analyses have relative accuracy of better than 5%.

4. Results: Sedimentology, facies analysis, and petrography

4.1. Kungarra Formation at Horseshoe Creek

Three parallel stratigraphic sections (HC1, HC2, and HC3) were measured from the Horseshoe Creek locality; as these sections were only a few hundred meters apart they are shown as a composite section in Fig. 2. The lower ~73.5 m consists of variably exposed, monotonous grey-green siltstone and shale with occasional thin (<10 cm) lenticular or planar beds of very fine- to fine-grained quartz-rich lithic arenites. These sandstone intervals are locally erosive and host parallel-lamination or occasional very fine ripple cross-lamination with abundant shale partings. Some of the more massive siltstone intervals are locally interspersed with starved ripples of very-fine grained sandstone, but many of the sedimentary structures in the siltstones are masked by a pervasive penetrative cleavage.

Numerous discontinuous limestone-bearing beds, 3–70 cm thick, occur sporadically within the massive siltstone and shale units. Many of these carbonate beds are broadly nodular or irregular in geometry and locally grade into pure siltstone, both vertically and laterally. Some carbonate-rich horizons essentially mimic starved ripples and other sedimentary structures characteristic of surrounding siliciclastic beds (Fig. 3A), consistent with post-depositional diagenetic carbonate precipitation. A diagenetic origin for these discontinuous layers is also supported by petrographic observations and microscale SEM-EDS mapping (Figs. 3C, 4). For example, evidence for diagenetic

246 carbonate emplacement includes both the restriction of these Kungarra carbonates to
247 lenses and thin layers intermixed with detrital grains (Figs. 3C, 4) and the distribution
248 within these lenses of patchy carbonate in overgrowth and cement-filling textures within
249 a matrix of silt-sized quartz grains, clay minerals, and rare other silicates (Figs. 3C, 4).
250 Figure 4 shows a representative carbonate layer (green) that includes many detrital
251 silicate grains (orange). A diagenetic origin for many Kungarra carbonates is consistent
252 with major element abundances reported by Lindsay and Brasier (2002); on average, Ca
253 and Mg together make up less than 15% by weight of sampled lithologies, requiring that
254 carbonates are a subordinate component of the samples.

255 A few limestone beds from the Kungarra Formation are more continuous,
256 relatively pure, and either irregularly laminated or clearly stromatolitic. In particular, a
257 distinct stromatolite unit occurs from ~33.9–34.4 m in section HC3, which progresses
258 from ~10 cm of brown-yellow-colored irregular crinkly lamination with interstitial
259 micrite fill into ~25 cm of discrete ~70 cm wide elongate stromatolites. These structures
260 are draped by peach-colored dolomicrite and transition into two distinct layers of
261 brownish-white ~15–30 cm thick domal stromatolites (Fig. 3B) separated by a horizon of
262 1–4 cm wide and ~10 cm tall, high-inheritance digitate stromatolites. The upper 2–5 cm
263 of the stromatolitic interval is irregular, with local rip-up clasts. Laterally, this
264 stromatolitic interval becomes poorly developed; at section HC2, only the irregular
265 carbonate laminae and small domal stromatolites occur (Fig. 3B), and at section HC1 this
266 unit becomes indistinguishable from other thin carbonate units. The only other location in
267 this section with similar stromatolitic features occurs at ~176 m; however, this microbial
268 unit is poorly developed and much thinner (~10 cm). Unlike the carbonate overgrowths in

the siltstone units, these carbonate units were likely primary (although they have since been recrystallized). Thus the carbonate-rich units at Horseshoe Creek reflect both original carbonate sediments as well as later carbonate overgrowths of siliciclastics.

The upper ~172 m of the Horseshoe Creek section broadly coarsens upwards into a siliciclastic succession dominated by very fine- to fine-grained sandstone. These strata generally transition from green-grey siltstone and argillite with abundant starved ripples, parallel lamination, ripple cross-lamination, and minor carbonate horizons into a succession dominated by very thin- to thin-bedded quartz-rich lithic arenite and sublitharenite with abundant shale partings. One can distinguish clear smaller-scale 1–5 m thick coarsening upwards packages of siltstone and shale into very-fine to fine-grained sandstone, which are superimposed on the broader coarsening upwards sequence on the formation scale.

4.2. Kazput Formation, NW Hardey Syncline

4.2.1. Kazput Section #1 (K1)

The K1 section (Figs. 5A, 6) was measured on the NE-dipping flank of a NNW-SSE-striking anticline in the southeastern part of the Hardey Syncline (locality 3 on Fig. 1). The base of this section is covered by alluvium, so its relationship to the underlying Koolbye Formation is unclear. The section begins with a prominent bench of dark grey parallel-laminated limestone, about 1.5 m thick (Fig. 5B), that is overlain by ~6 m of sandy limestone with evidence for soft-sediment deformation. The carbonate strata become increasingly sand-rich and dolomitic upsection until, by ~16.5 m, they are dominated by medium-bedded brown dolomitic sandstone. The outcrop then disappears

292 into cover for ~30 meters, but thin-bedded, often calcareous, sandstone horizons are
293 occasionally visible in subcrop (Fig. 5A). Continuous outcrop reappears at 52.5 m, again
294 consisting of interbedded finely laminated calcareous sandstone and brown
295 dolograinstone. The overlying 30 m consists of brown-weathering (white on fresh
296 surface), coarsely recrystallized dolomite with no visible sedimentary structures. At 86.8
297 m the recrystallization fabric disappears and dolostone displays crinkly lamination and
298 roll-up structures that resemble microbially influenced sedimentary structures. In
299 addition, interbedded chert-replaced rip-ups and intraformational conglomerates occur
300 with other indicators of traction load deposition, including ripple and trough cross-
301 stratified dolograinstone, channelized grainstone, and thin channelized sandstone lenses
302 (Fig. 5C). Starting at 116.7 m, the section becomes dominated by wavy laminated
303 dolomite, with abundant pisoids and oncoids (up to a cm in diameter), and domal
304 stromatolites up to 30–50 cm wide. A small fault cuts the section at ~127.5 m rendering
305 thickness measurements of the uppermost part of the succession less reliable. At a
306 minimum, an additional 10 m of small conical stromatolites, oncoids, and massive grey
307 dolomite cap the section. Pervasive recrystallization of Kazput Formation carbonates
308 dominates petrographic fabrics, but the interlocking calcite euhedra still preserve mm-
309 scale features such as bedding lamination, coated grains, and ooids.
310
311 *4.2.2 Kazput Section #2 (K2)*
312 The K2 composite section (Figs. 7A, 8, 9) was measured on the SW-dipping flank
313 of the anticline in the central part of the Hardey Syncline (Locality 2 on Fig. 1). The K2
314 section includes two ridges (Fig. 7A) separated by a small valley filled by alluvial

315 material (likely the surficial expression of a fault), so the stratigraphy is represented
316 herein as a composite section (K2A, K2A2, and K2B–K2C; Figs. 8, 9).
317 The basal portion of section K2A (Fig. 8) consists of highly fractured and
318 oxidized maroon and olive green siltstone and shale subcrop exposed in a small, south-
319 flowing dry creek bed at the core of the anticline. Fine-grained deposits transition
320 upsection into ~18 m of olive green to dark grey, parallel laminated to ripple cross-
321 laminated micritic limestone with locally-abundant silt and very fine-grained quartz sand.
322 The basal carbonate-rich strata are thinly bedded and record discrete mm- to cm-scale
323 alternations between massive and laminated beds that resemble the discrete Bouma C-E
324 subdivisions of distal turbidites. The central ~6 m of these more carbonate-rich strata are
325 dominated by pure olive green siltstone with minor detrital carbonate, and the upper 5–6
326 m of these strata record the local development of hummocky cross-stratification and
327 occasional stoss-preservational ripple cross-lamination in the silty limestone deposits.
328 The upper ~45 m of section K2A consists of a broad coarsening-upwards package of
329 olive green to dark grey siltstone and argillite and minor thin-bedded light brown very-
330 fine- to fine-grained quartz sandstone (Fig. 7B). The sandstone beds generally display
331 evidence for subtle scouring of underlying siltstone and argillite intervals and the units
332 are dominated by hummocky and swaley cross-stratification. Sedimentary structures in
333 the siltstone and argillite strata are difficult to discern due to a pervasive penetrative
334 cleavage, but they occasionally contain thin (< 5 cm thick) stringers of nodular and planar
335 micritic limestone. The silica- and carbonate-cemented sandstones of the Kazput
336 Formation can generally be classified as quartz-rich sublitharenites (Martin et al., 2000),

337 but they are mostly dominated by moderately sorted and subrounded to angular
338 monocrystalline quartz sand with minor lithics, chert, and a pervasive chloritic matrix.
339 Since the upper part of section K2A was exposed on a prominent dip slope that
340 projected into a small, faulted alluvial valley, a parallel section was measured to the
341 northwest on the other side of the structure, section K2A2 (Fig. 8). A ~6 m thick package
342 of pure olive green siltstone was used to trace the section over the projected small fault
343 horizon. This section begins with ~17 m of dark grey-green siltstone and argillite that
344 progressively becomes increasingly carbonate rich. Thin (2–3 cm thick) stringers of
345 nodular to stratiform, silty micritic limestone thicken upsection into parallel-laminated
346 and ripple cross-laminated beds up to 10 cm thick. These silty limestone deposits are
347 abruptly overlain by ~4 m of peach-orange to blue-grey-colored fine-grained
348 dolograinstone with abundant ripple cross-lamination and minor detrital silt and quartz
349 sand. Locally, there are thin (<20 cm) horizons with irregular and wavy lamination that
350 resemble microbial carbonates. The upper portion of this small section becomes heavily
351 dolomitized, although there are multiple horizons with crenulated or wavy laminae and
352 intervals of detrital silt and quartz sand that form discrete lenses and stringers within the
353 carbonate laminae. A massive, light bluish-grey colored dolostone horizon was used to
354 trace this section over to section K2B.
355 Section K2B forms the base of a large hill and K2B/C comprises over 65 m of
356 interbedded carbonate and siliciclastic deposits with some evidence for synsedimentary
357 slumping and faulting (Figs. 7A, D, 9). The lowermost 21 m of K2B strata are composed
358 of silty to fine-grained sandy limestone with mm-scale parallel lamination, ripple cross-
359 lamination, and low-angle bedding truncations (Fig. 7B) interbedded with two carbonate-

dominated units: a) fine-grained micritic limestones with wavy laminae, crenulated laminae, and small slumps from syn-sedimentary faults; and b) finely-laminated silty to sandy carbonates with low angle hummocky and swaley cross stratification (Fig. 7C). The wavy laminated carbonates often form thin (up to a few cm) stromatolites, which can follow relict topography (Fig. 10B) or become contorted, folded, or faulted (syn-sedimentary). These cm-scale stromatolite layers become thicker and well developed higher in the section. Above the interbedded silty and stromatolitic carbonates is a thick (~15 m) interval of well-sorted, fine- to medium-grained sandstone, in decimeter-scale beds with ripple and hummocky cross-stratification.

A similar succession of silty and stromatolitic carbonates capped by thick sandstone occurs again in the K2C section; however, the internal structure of the silty carbonate is more massive than those lower in the section. Higher in the section (around 45 m), the stromatolitic units develop into thick, well-defined, meter-scale stromatolite domes (Fig. 10). These large stromatolites are commonly contorted and occasionally cut by neptunian dykes (e.g. Fig. 10E). Interbedded with and above the large stromatolitic domes are wave-rippled and hummocky cross-stratified silty sandstones. Beds are often amalgamated, making bedding thickness difficult to discern. A further silty sandstone at the top of the section is distinguished by carbonate intraclasts one centimeter to several meters in length and typically rounded or tabular in shape (Fig. 9). The clasts consist of stromatolites and other carbonate lithologies observed lower in the section, as well as recrystallized oolitic grainstones that broadly link the two measured Kazput sections.

5. Results: *Carbon isotope chemostratigraphy*

383 *5.1. Kungarra carbonates*

384 Lindsay and Brasier (2002) reported carbon isotopic abundances for 22 carbonate
385 samples distributed through an estimated 250 m of stratigraphy at Horseshoe Creek,
386 reported as Kazput Formation but now known to belong to the Kungarra Formation.
387 Their $\delta^{13}C$ values ranged from -6 to +2‰, varying in sawtooth fashion through the
388 reported section. Our larger sample set (n = 125) is consistent with measurements by
389 Lindsay and Brasier (2002); $\delta^{13}C$ values for Kungarra carbonates at Horseshoe Creek
390 exhibit a wide range of isotopic values, from -6.3‰ to +0.5‰, with no strong
391 stratigraphic trend (Fig. 2). The $\delta^{18}O$ values for the same samples range from -6.15‰ to -
392 1.61‰, again with no strong trend (see supplemental data). In contrast to Lindsay and
393 Brasier (2002), our denser sampling coverage across multiple spatial scales enables us to
394 detect variations in the carbon isotope results of up to 2‰ between lighter (more
395 carbonate) and darker (less carbonate) layers within a single hand sample, as much as 4‰
396 between samples from closely spaced sections at a single stratigraphic horizon, and
397 equally strong variation between samples spaced stratigraphically only centimeters to a
398 few meters apart (Fig. 2, supplemental data).
399
400 *5.2. Kazput carbonates*

401 All $\delta^{13}C$ values measured for Kazput carbonates in the Hardey Syncline (n = 252)
402 fall between -4.5‰ and +2‰, and all but a stratigraphically constrained subset lie
403 between -0.5‰ and +1.5‰ (Figs. 6, 8, 9). These results are consistent with
404 reconnaissance analyses by Bekker et al. (2002). $\delta^{18}O$ values range from -8.13‰ to -
405 16.63‰, with most values falling between -15.5‰ and -16.5‰ (see supplemental data).

406 At the base of section K1 (Fig. 6), $\delta^{13}C_{carb}$ values are low (around -4‰); whereas
407 the last data point before the prominent covered interval is more moderate at 0.7‰.
408 Above the covered interval, $\delta^{13}C_{carb}$ values are again depleted (-3‰) but quickly return to
409 values between 0 and 1‰ for the remainder of the section (Fig. 6). The $\delta^{13}C_{carb}$ signature
410 of section K2 begins much like that of K1, with negative values (-2.5‰ to -1.2‰) in the
411 lowermost 10 m (K2A, Fig. 8) followed by values that fluctuate around 0‰ (K2A and
412 K2A2, Fig. 8). Higher in the section (K2B and K2C), C-isotopic values generally
413 fluctuate between ca. 0.5 and 1.5‰, with a few more negative values interspersed
414 through the sections (Fig. 9). Variations of up to 1‰ among carbonate intraclasts at the
415 top of the section likely reflect the heterogeneous stratigraphic levels from which the
416 intraclasts and carbonate blocks were sourced.
417 Petrographic subsampling of stromatolites at 46–47 m of K2C shows limited
418 isotopic variation among microfacies, with stromatolitic carbonates slightly heavier than
419 the carbonate-rich clastics that overlie the stromatolites (Fig. 9). As might be predicted
420 when ambient waters are strongly oversaturated with respect to calcite and aragonite
421 (Bergmann et al., 2013), carbonates within stromatolites differ little from encompassing
422 laminae in both their carbon and oxygen isotope values (Fig. 9). The analyzed Kazput
423 carbonates do not record the extreme ^{13}C enrichment that defines the younger
424 Lomagundi-Jatuli event.
425
426 ***6. Results: Kazput stromatolites***
427 The most notable sedimentary features of the Kazput carbonates are m-scale
428 domal stromatolites in section K2B/C (Fig. 10). These stromatolites appear to have

nucleated on erosional surfaces within underlying siliciclastic units and were, in turn, episodically buried by further influx of sands that locally display hummocky cross-stratification. The resulting microbialites can be as thin as a centimeter (Fig 10B), suggesting only a limited time for accretion between inundation events, to as much as 1.5 meters thick (Fig 10A).

Two fabrics make up the Kazput stromatolites (see Section 7.3 for genetic interpretations): wavy to crenulated siliciclastic laminae, 30 to 400 μm thick, that are continuous on the scale of a single dome, and interbedded, convex upward, lenticular carbonates that are generally discontinuous on a mm to cm-scale and are common or absent in alternating zones (Fig. 10). The discrete fabrics are clear in both optical microscopic view (Fig. 11) and in elemental maps using SEM (Fig. 12). Lamina-rich zones tend to be <1 cm to about 2 cm thick, whereas zones rich in lenticular carbonate vary from <1 cm to, more commonly, 10–15 cm thick. Because silicate laminae are more resistant to erosion than carbonate lenses, the broad mesoscale fabric of the stromatolites is best observed on weathered surfaces; lamina-rich zones are darker brown and more resistant, carbonate-rich zones are grey or lighter tan and more recessive (Fig. 10). For the most part, lenticular carbonates occur within 5–15 mm long convex-upward mini-domes bounded by laterally linked laminae that tend to be continuous across the surfaces on which they occur. In some layers, lenses extend laterally for several cm along bedding planes (Fig 10D); however, these occurrences are rare. Most of the stromatolitic structures are irregular, and some show evidence of plastic deformation (folds and slumps). At a few horizons, however, more or less regular, laterally linked columns

451 develop either locally (Fig. 10F) or across a stromatolitic dome surface (Fig 10D);
452 columns are 5–8 cm wide and 2–10 cm high.

453 At the microscopic scale, laminae contain an admixture of several minerals,
454 including equant calcite anhedra, 10–25 μm in maximum dimension; quartz silt; clay
455 minerals (commonly chloritized, but also including Mg-rich species); and small opaque
456 euhedra, probably originally diagenetic pyrite, but now altered to iron oxides (Figs. 11,
457 12). While clays can form authigenically within microbialites (Konhauser and Urrutia,
458 1999; Léveillé et al., 2000) the presence of abundant fine-grained quartz grains and other
459 detrital material indicates the incorporation of suspension load siliciclastics, even when
460 traction load sands were absent. Organic carbon inclusions also occur sporadically
461 throughout the K2 stromatolites; these appear as black spots on the composite elemental
462 map or red spots on the carbon map in Figure 12.

463 Lenticular units generally consist of interlocking calcite anhedra 25–100 μm in
464 maximum dimension. Pyrite, reduced carbon, and clay minerals also occur in these zones,
465 although at low abundances (Fig. 12). The coarsely crystalline carbonates reflect
466 pervasive diagenetic and/or metamorphic recrystallization, but mm-scale banding is
467 preserved locally (Fig 11C). Crystals are smaller in these banded carbonates, generally
468 less than 25 μm, and discrete zones are defined by both larger and smaller crystals
469 (lighter and darker zones in Fig 11C), as well as a faint tendency for smaller crystals to be
470 oriented along laminae surfaces.

471 The stromatolites form irregular, m-scale domes on flat-lying surfaces or arches
472 over relict seafloor relief; local reorientation and folding indicate slumping during or
473 shortly after accretion. Like the smaller scale fabrics, at the decimeter to meter scale these

stromatolitic domes are variable in shape, but heritability is much higher. The domes are capped by and often interbedded with hummocky cross-stratified sandstones. Clastic-filled neptunian dykes occur sporadically through the section (Fig. 10E). The dykes typically cut at a high angle through the undeformed stromatolite layers, but can run parallel to lamination in cement-poor intervals. In aggregate, these features are plausibly explained by a composite structure that combined rigid penecontemporaneous cements with more plastic silt- and clay-rich laminae, as discussed below.

7. Discussion

7.1 Kungarra carbonates

Broadly, Kungarra Formation strata record a major coarsening upwards sequence from banded iron formation and starved basin deposits of the underlying Boolgeeda Iron Formation through glaciomarine deposits of the Meteorite Bore Member and finally into tidal flat, beach, and fluvial deposits of the overlying Koolbye Formation (Mazumder et al., 2015). The measured Horseshoe Creek section (Fig. 2) captures a small component of this broad coarsening upwards trend. The abundance of fine-grained suspension deposits interbedded with starved ripple and planar ripple cross-laminated sandstone intervals most likely represents subtidal deposition between storm and fair weather wave base. This is consistent with the limited development of stromatolites. The lack of directly overlying shoreface deposits suggests that deposition was predominantly in an offshore setting, although the increase in sandstone intervals and the broad coarsening upwards trend in the upper ~25 m of the measured section is diagnostic of progradation. Given these features, we suggest these strata were largely deposited in a prodeltaic or mid-outer

497 shelf environment, broadly consistent with the interpretations of previous workers
498 (Krapež, 1996; Martin et al., 2000; Van Kranendonk et al., 2015).

499 As noted above, Lindsay and Brasier (2002) sampled the carbonate-bearing rocks
500 at Horseshoe Creek, and the highly variable carbon isotope values were interpreted to
501 indicate pronounced carbon cycle variation in the aftermath of the GOE. However,
502 regional mapping has shown that the strata in question lie stratigraphically beneath the
503 Meteorite Bore Member and so are properly assigned to the Kungarra Formation
504 (Krapež, 1996; Martin et al., 2000; Van Kranendonk et al., 2015). Furthermore,
505 stratigraphic field relationships and detailed petrology both suggest that most of these
506 Kungarra carbonates formed during diagenesis, and the marked C-isotopic variation
507 recorded in these rocks confirms this interpretation (Figs 2–4). $\delta^{13}C$ values of -6‰ are
508 unusual for carbonates of any age and commonly reflect the incorporation of isotopically
509 light carbon into diagenetic carbonates precipitated within sediments (Irwin et al., 1977).
510 Within Lindsay and Brasier's (2002) plotted stratigraphic column, $\delta^{13}C$ values commonly
511 vary by several per mil from one sample to the next. Our more detailed data set enables
512 us to document large carbon isotopic variations (up to 4‰) within hand samples and
513 between samples from the same stratigraphic horizon (Fig. 2). Such fine-scale spatial and
514 temporal variation is essentially impossible to accommodate in terms of primary C-
515 isotopic signatures reflecting global seawater chemistry.

516 Arguably, the isotopic variation observed at individual horizons in the lower
517 Kungarra Formation of the Horseshoe Creek section reflects diagenetic carbonate
518 precipitation from pore fluids in which dissolved inorganic carbon (DIC) sourced from
519 seawater was variably mixed with inorganic carbon generated by the remineralization of

520 isotopically light organic matter. In this case, the most positive isotope results represent
521 values closest to the dissolved inorganic carbon (DIC) in seawater. Alternatively, if these
522 units underwent episodic subaerial exposure in the Paleoproterozoic, meteoric waters
523 may have altered the isotopic composition of the strata during early diagenesis.
524 Regardless, the isotopic values from the measured Kungarra Formation from the
525 Horseshoe Creek section by and large do not represent the original isotopic composition
526 of seawater during the time of deposition.
527
528 *7.2. Kazput carbonates*
529 Similar to the underlying Kungarra Formation, the ~750 m thick Kazput
530 Formation records a complex depositional history heavily influenced by local
531 synsedimentary tectonism (Krapež, 1996; Martin et al., 2000; Thorne and Tyler, 1996;
532 Thorne et al., 1995). Numerous cm to dm scale synsedimentary normal faults in K2B and
533 K2C indicate the occurrence of active extensional tectonism during Kazput
534 sedimentation. Furthermore, the large stromatolitic clasts and rip-ups (including m-scale
535 rafts that are clearly transported) in the uppermost K2 facies likely represent seismically-
536 generated breccias (seismites) or the erosion of locally uplifted strata. Given the limited
537 stratigraphic range of this study within the Turee Creek Group, it is difficult to provide
538 more context to the greater basinal or tectonic setting of these strata.
539 Given previous descriptions of the basal Kazput succession as a starved basin
540 marked by distinct carbonate rhythmites (e.g., Krapež, 1996), the Kazput sections
541 described here appear to lie relatively close to the base of the formation. The parallel-
542 laminated and turbiditic silty limestone units that mark the base of the two measured

543 sections suggest a relatively quiet-water environment. At both localities, the rocks
544 quickly transition upsection into fine-grained siliciclastic units with abundant evidence
545 for storm-generated bedforms, indicative of higher energy/shallower water conditions.
546 The remainder of the measured sections can be interpreted as a broad shallowing upward
547 succession of mixed carbonate and siliciclastic strata. The abundance of fine-grained
548 shale and siltstone interbedded with hummocky and swaley cross-stratification in the
549 central part of the sections suggests subtidal deposition on a storm-dominated shelf
550 between storm and fair weather wave base. The establishment of this subtidal shelf
551 setting was relatively short-lived because both Kazput sections record relatively abrupt
552 shoaling into shallow-water shoreface and platformal settings. This is clearly evidenced
553 by the deposition of thick peritidal to subtidal platformal carbonate dominated by ooids,
554 oncoids, and coarse dolograinstone in section K1 (Fig. 6) and a more complex mixed
555 sandstone-stromatolitic limestone sequence in section K2 (Figs. 8, 9).
556 The striking difference in siliciclastic composition between the upper portions of
557 the two parallel sections (K1 and K2) is problematic; however, given the complexity and
558 heterogeneity of along-strike facies and possible proximity to a shoreline, it is reasonable
559 to conclude that their differences are primarily due to proximity to siliciclastic point
560 sources, such as nearby deltaic systems. In fact, section K2 preserves many of the
561 hallmarks of high sedimentation rates in a tectonically active basin, such as thick
562 sequences of stoss-preservational ripple cross-lamination and abundant synsedimentary
563 dykes and soft-sediment deformation. The intimate association of unique stromatolite
564 morphologies and abundant trough cross-stratified sandstone intervals in the upper K2
565 interval also suggests deposition in a shoreface setting subject to periodically high

566 sedimentation rates. We note that carbonate lithologies differ between sections K1 and
567 K2, with stromatolite development limited to the latter. We cannot rule out the possibility
568 that the two sections are not strictly coeval, but prefer to interpret these facies as
569 contemporaneous expressions of carbonate deposition in a spatially heterogeneous and
570 rapidly developing basin.

571 Unlike the results from the Kungarra Formation carbonates, the Kazput isotope
572 data are interpreted to indicate dominantly primary seawater values. The agreement of
573 values from closely spaced samples and the consistent trends suggest that diagenetic
574 overprinting of the isotopic signal was minimal. Furthermore, no petrographic results
575 suggest secondary calcite overgrowths, which are clearly documented in the Kungarra
576 carbonates (Fig. 3). Thus, the C-isotopic values of -1 to -3‰ in lowermost Kazput
577 carbonates could record transiently low $\delta^{13}C$ in contemporaneous seawater. Above this
578 horizon, however, values hover between 0.5‰ and 1.5‰ through the reminder of the
579 succession.

580

581 *7.3. Kazput stromatolites*

582 The striking m-scale stromatolite domes of the Kazput Formation (Fig. 10) exhibit
583 features that are typically associated with microbial carbonates, but are unique in
584 containing such an abundance of lensoidal calcite precipitates. Laminae in these
585 structures are interpreted as the sedimentary manifestation of mat-building microbial
586 communities. Beyond their general similarity to laminae observed in stromatolites
587 throughout the Proterozoic Eon, a mat origin is supported by at least four observations:
588 (1) the irregular and commonly distorted surfaces of laminae indicate formation by

materials that were both coherent and flexible; (2) quartz silt and, very likely, clay minerals within laminae indicate the trapping and binding of introduced materials; (3) laminae contain a higher concentration of reduced carbon than associated microfabrics, consistent with an origin as mats; and (4) laminae contain localized high concentration of (originally) pyrite, suggesting decay within mats via microbial sulfate reduction. The microbial mats likely nucleated on sandy substrates, forming wrinkled mats (wrinkle structures or laminae) and cm-scale stromatolites (Fig 10B); larger structures resulted from protracted growth between episodes of sand deposition. Based on petrographic and elemental analysis, the quartz silt and clay minerals that are found within the stromatolites indicate that suspension load siliciclastics were continuously deposited on mat surfaces during stromatolite growth.

An outstanding question is the extent to which the lenticular carbonates found between laminae formed on, or just beneath, mat surfaces or filled primary voids formed by gas emission within mats. Gas-generated voids occur sporadically throughout the Proterozoic stromatolite record. Their formation generally requires strong but flexible mats populated by filamentous microorganisms, gas generation (e.g., oxygenic photosynthesis, decomposition of organic matter, or methanogenesis), and seawater that is strongly oversaturated with respect to calcium carbonate minerals (e.g., Knoll et al., 2013; Mata et al., 2012). Indeed, primary voids in Archean stromatolites have been interpreted as prima facie evidence for oxygenic photosynthesis at 3 Ga (Bosak et al., 2009, 2010). The carbonate precipitates do not crosscut microbial laminae, eliminating dissolution and subsequent in-filling as an explanation for the observed textures.

611 Given that the Kazput stromatolites lie within rocks deposited stratigraphically
612 after the GOE, all aforementioned requirements for the formation and preservation of
613 primary voids appear to have been met locally. The irregular, convex upward
614 morphology of laminae is consistent with this interpretation, as is the orientation of zoned
615 cements in some stromatolites (Fig. 11C, E). However, the lateral extent of discrete
616 cement horizons that occasionally contain clay, pyrite, and reduced carbon flecks also
617 supports the alternative interpretation that the cements are seafloor precipitates formed on
618 or within surface mats (e.g., Fig. 11B). In fact, the two interpretations are not mutually
619 exclusive; if the waters that bathed the Kazput bioherms were strongly supersaturated
620 with respect to calcium carbonate, both void-forming and cementing processes may have
621 been operating during stromatolite accretion.
622 Stromatolites are found widely in late Archean and Paleoproterozoic carbonates,
623 with particularly good descriptions of macro- and microstructure available for late
624 Archean microbialites from the Gamohaan and Frisco formations of the
625 Campbellrand/Malmani succession, South Africa (Sumner, 1997), and lower
626 Paleoproterozoic carbonates from the Fennoscandian Shield (McLoughlin et al., 2013).
627 What differentiates the Kazput stromatolites from most of these (and essentially all
628 younger Proterozoic) structures is their abundance of lenticular carbonate. Microdigitate
629 stromatolites, some of them small microbial structures and others stacked crystal fans
630 (Grotzinger and Knoll, 1999), are particularly widespread in Paleoproterozoic carbonate
631 successions (Medvedev et al., 2005). These structures formed widely across shallow
632 shelves and platforms and reflect a high degree of oversaturation with respect to calcium
633 carbonate minerals. Thus, they are relevant to the interpretation of the Kazput structures,

634 but differ in lacking the regular interlamination of microbial laminae and precipitates
635 described here.
636 Perhaps the closest approximation of the composite laminar-lenticular Kazput
637 fabric is found in cuspate microbialites from the Campbellrand/Malmani succession
638 (Sumner, 1997) and elsewhere in late Archean carbonates (e.g., Hofmann and Masson,
639 1994; Riding et al., 2014). In these structures, void spaces that originated by the draping
640 of pliant mats across vertical microbial "tent poles" were filled penecontemporaneously
641 by carbonate cement (Sumner, 1997). Locally, stromatolites in the 2720 ± 5 Ma
642 Tumbiana Formation, Fortescue Group, Western Australia, also contain thin, irregular
643 patches of carbonate precipitates, interpreted as lake-floor precipitates (Flannery and
644 Walter, 2012; Lepot et al., 2008, 2009). The Kazput and Tumbiana stromatolites do share
645 some similarities, such as the weathering profile (prominent laminae and recessive
646 cements) and the μm-scale banded carbonate domes within carbonate-rich layers;
647 however, there are important distinctions between the two. Kazput stromatolites do not
648 contain halite pseudomorphs, nor is there evidence for the penecontemporaneous erosion
649 of carbonate precipitates, as is clearly evident in the Tumbiana stromatolites (Lepot et al.,
650 2008, 2009). Furthermore, the Kazput stromatolites cements are largely discrete (mm- to
651 cm-scale) lenses and typically do not form thick, continuous cement laminae as in the
652 Tumbiana examples. These examples underscore the importance of macroscopic
653 carbonate precipitates in generating fabrics within late Archean/early Paleoproterozoic
654 stromatolites; nonetheless, the specific alternation of particle-binding mats and lenticular
655 carbonate precipitates is, to the best of our knowledge, a unique feature of Kazput

656 stromatolites in the Hardey Syncline, reflecting a potentially time-limited interaction
657 between the evolving biota and its physical surroundings.
658
659 *7.4. Chemostratigraphic comparisons*
660 Few carbon isotopic data are available for carbonates that unambiguously lie
661 above Paleoproterozic iron formations but below glaciogenic rocks. Samples from the
662 poorly dated Boxelder Creek Formation, South Dakota (Bekker et al., 2003a) and
663 Polisarka Sedimentary Formation in drill cores from the Kola Peninsula, Russia (Brasier
664 et al., 2013), span a range of -6‰ to 1‰. Carbonates of the Gandarela Formation, Brazil,
665 are isotopically similar, but cannot be placed unambiguously relative to Paleoproterozoic
666 ice ages. Post-glacial marbles of the Paleoproterozoic Sauser Group, India, also show C-
667 isotopic values of -3.1‰ to +2.6‰ above a moderately negative basal interval (-4.4‰ to
668 -7.4‰) interpreted as a cap carbonate (Mohanty et al., 2015). The most positive C-
669 isotopic values for Kungarra carbonates are consistent with the values reported from
670 other basins, but the uncertainties introduced by diagenetic carbonate precipitation limit
671 what the Kungarra samples can add to discussions about the post-BIF, pre-GOE carbon
672 cycle.
673 On the basis of limited data, Karhu and Holland (1996) hypothesized that the
674 strongly positive carbon isotopic excursion called the Lomagundi-Jatuli event began ca.
675 2.2 Ga. Even now, isotopic data are sparse for successions younger than GOE
676 onset/glaciogenic rocks but older than 2200 Ma. Martin et al. (2013) summarized
677 available radiometric constraints on the Lomagundi-Jatuli event, concluding that the
678 event began between 2306 ± 9 Ma and 2221 ± 5 Ma and ended between 2106 ± 8 and

679 2057 ± 1 Ma, for a maximum duration of 249 ± 9 million years and a minimum duration
680 of 128 ± 9.4 million years. The new data presented herein are consistent with these age
681 constraints, and provide no evidence for strongly positive Lomagundi-Jatuli $\delta^{13}C$ values
682 during deposition of the measured Kazput sections. We recognize, however, that our
683 sections represent a limited proportion of the time interval between Paleoproterozoic ice
684 ages and events commencing at 2200 Ma; regionally, Kazput carbonates are separated
685 from the Cheela Springs basalt and its intrusive counterpart (2209 ± 15 Ma; Martin et al.,
686 1998) by thick siliciclastic deposits and a major unconformity (Fig. 1). Thus, while these
687 new data demonstrate that the interval between the GOE onset/glacials and 2200 Ma
688 includes a time where the seawater DIC isotopic composition was unperturbed and
689 similar to modern isotopic values, we cannot rule out the possibility that it also includes
690 short intervals of positive C-isotopic excursions, which are not recorded in the analyzed
691 Kazput Formation sections.
692 Kazput carbonates are isotopically similar to those of well-developed carbonates
693 in the Gandarela Formation, Brazil, where 163 samples show values near 0‰ (Bekker et
694 al., 2003b; Maheshwari et al., 2010). The Gandarela carbonates (Babinski et al., 1995) lie
695 stratigraphically above major BIF and below carbonates that show Lomagundi-type ^{13}C
696 enrichment, but the regional stratigraphy contains no glacial diamictites; Bekker et al.
697 (2003b) cite a Pb-Pb date of 2420 ± 19 Ma for Gandarela carbonates, but this does not
698 appear in Martin et al.'s (2013) review due to the low confidence in the interpretation of
699 Pb-Pb carbonate dates in Proterozoic successions. The well-studied Duitschland
700 Formation, dated indirectly at 2316 ± 7 Ma by Re-Os on black shale of the possibly
701 correlative Rooihoogte-Timeball Hill Formation (Hannah et al., 2004), bears ^{13}C

enrichments up to 10.1‰ in its upper part (Bekker et al., 2001). However, the Mooidraai Dolomite (diagenetic age of 2394 ± 26 Ma, based on carbonate-bound Pb), also in South Africa, appears to have no isotopic anomalies, with $\delta^{13}C$ values of 0.5 to 1‰, more similar to those of the Kazput Formation (Bau et al., 1999). Clearly, tighter radiometric constraints will be necessary to validate interbasinal correlations and accurately reconstruct early Paleoproterozoic carbon cycle dynamics.

8. Conclusions

This study provides new litho- and chemostratigraphic data for carbonate-bearing intervals of the 2.45–2.22 Ga Turee Creek Group, Western Australia, which spans a pivotal time in Earth history after the deposition of global banded iron formation and across the GOE. Field relationships, petrography, elemental mapping, and C-isotope values reveal that most Kungarra carbonates in the pre-glacial lower part of the Turee Creek Group formed during syndepositional or post-depositional diagenesis; therefore, the abundant and highly negative C-isotopic values within these rocks cannot be interpreted in terms of global carbon cycle dynamics, as previously assumed by Lindsay and Brasier (2002).

In contrast, carbonates from the lower part of the uppermost Kazput Formation of the Turee Creek Group — which sits in a globally under-sampled interval above Paleoproterozoic glacial deposits and below an unconformity constrained by the ~2.2 Ga Cheela Springs Basalt and associated sills — do appear to record the C isotopic composition of seawater DIC, with consistent $\delta^{13}C$ values of -2 to +1.5‰. As the lower parts of the Kazput Formation likely represent a relatively brief time interval, it

725 strengthens a growing body of evidence indicating that the initial geochemical signature
726 of the GOE and the exceptionally positive values of the Lomagundi-Jatuli isotope
727 excursion(s) are separated by one or more intervals of normal C isotopic composition.
728 The moderate C-isotopic values of Turee Creek Group carbonates strengthen the
729 argument that the complex set of processes that drove the onset of the GOE did not
730 include anomalously high proportional rates of organic carbon burial. Of course, as others
731 have noted (e.g., Lyons et al., 2014; and references therein), it is not required that the
732 increase in Paleoproterozoic oxygen concentrations was limited to the brief interval
733 marked by the end of mass-independent S isotope fractionation, nor that oxygen change
734 was monotonic (Canfield, 2014; Canfield et al., 2013; Lyons et al., 2014). Instead, the
735 MIF-S signature might reflect an interval of atmospheric oxygen accumulation that was
736 neither large nor rapid but crossed an important threshold. One would expect pO_2 to
737 continue to rise during the Lomagundi-Jatuli event (e.g., Bekker and Holland, 2012;
738 Kump et al., 2011; Rasmussen et al., 2013), but any increase in oxygen levels driven by
739 extensive organic carbon burial postdates the MIF-S boundary, very likely by tens of
740 millions of years (see also Martin et al., 2013).
741 Beyond the perspective on Paleoproterozoic carbon cycle dynamics provided by
742 the stable carbon isotopic data, Turee Creek Group carbonates host unusual, if not
743 unique, stromatolites that are geobiologically informative. Notably, Kazput stromatolites
744 contain a high volume of precipitated carbonate—indeed, more abundant than the
745 siliciclastic-rich laminae in many horizons (Fig. 10). As noted above, this reflects locally
746 abundant seafloor precipitates and/or penecontemporaneous filling of primary voids
747 formed by microbial gas release. The most comparable structures are precipitate-rich

748 cuspate Archean microbialites from South Africa (Sumner, 1997) and late Archean
749 Tumbiana stromatolites from Western Australia (Flannery and Walter, 2012; Lepot et al.,
750 2008, 2009). Whatever their proper mechanistic interpretation, the Kazput Formation
751 stromatolites in the Hardey Syncline are morphologically distinct, reflecting a potentially
752 time-limited interaction between the evolving biota and its physical surroundings.
753

754 **Acknowledgements**

755 We thank R. Shapiro and an anonymous reviewer for constructive comments on
756 an earlier version of this paper. We thank the Agouron Institute for funding the 2012
757 Advanced Geobiology Course to Australia, Henry Goodall and Guy L'Estrange for
758 logistical support, and Sarah Manley for running the carbon isotope analyses. R.
759 Martindale thanks Dr. A. H. Knoll and the NASA Astrobiological Institute for providing
760 postdoctoral funding. J. Strauss and K. French acknowledge NSF graduate research
761 fellowships for funding support. E. Sperling thanks the Agouron Institute for an Agouron
762 Postdoctoral Fellowship. D. Flannery was supported by the University of New South
763 Wales and the Australian Centre for Astrobiology. M. Walter acknowledges a
764 Professorial Fellowship from the Australian Research Council. R. Mazumder is grateful
765 to the University of New South Wales and Agouron Institute for support. M. Van
766 Kranendonk also acknowledges funding support from the University of New South
767 Wales.

768 **References**

769 Akin, S.J., Pufahl, P.K., Hiatt, E.E., Pirajno, F., 2013. Oxygenation of shallow marine
770 environments and chemical sedimentation in Paleoproterozoic peritidal settings: Frere
771 Formation, Western Australia. Sedimentology 60, 1559-1582.
772 Asael, D., Tissot, F.L.H., Reinhard, C.T., Rouxel, O., Dauphas, N., Lyons, T.W.,
773 Ponzevera, E., Liorzou, C., Chéron, S., 2013. Coupled molybdenum, iron and uranium
774 stable isotopes as oceanic paleoredox proxies during the Paleoproterozoic Shunga Event.
775 Chemical Geology 362, 193-210.
776 Babinski, M., Chemale Jr, F., Van Schmus, W.R., 1995. The Pb/Pb age of the Minas
777 Supergroup carbonate rocks, Quadrilátero Ferrífero, Brazil. Precambrian Research 72,
778 235-245.
779 Barley, M.E., Pickard, A.L., Sylvester, P.J., 1997. Emplacement of a large igneous
780 province as a possible cause of banded iron formation 2.45 billion years ago. Nature 385,
781 55–58.
782 Bau, M., Romer, R.L., Lüders, V., Beukes, N.J., 1999. Pb, O, and C isotopes in silicified
783 Mooidraai dolomite (Transvaal Supergroup, South Africa): implications for the
784 composition of Paleoproterozoic seawater and ‘dating’ the increase of oxygen in the
785 Precambrian atmosphere. Earth and Planetary Science Letters 174, 43-57.
786 Bekker, A., Holland, H.D., 2012. Oxygen overshoot and recovery during the early
787 Paleoproterozoic. Earth and Planetary Science Letters 317–318, 295-304.
788 Bekker, A., Holland, H.D., Wang, P.-L., Rumble, D., Stein, H.J., Hannah, J.L., Coetzee,
789 L.L., Beukes, N.J., 2004. Dating the rise of atmospheric oxygen. Nature 427, 117-120.

790 Bekker, A., Karhu, J.A., Eriksson, K.A., Kaufman, A.J., 2003a. Chemostratigraphy of
791 Paleoproterozoic carbonate successions of the Wyoming Craton: tectonic forcing of
792 biogeochemical change? Precambrian Research 120, 279-325.
793 Bekker, A., Kasting, J., Anbar, A., 2013. Evolution of the atmosphere and ocean through
794 time. Chemical Geology 362, 1-2.
795 Bekker, A., Kaufman, A.J., Karhu, J.A., Beukes, N.J., Swart, Q.D., Coetzee, L.L.,
796 Eriksson, K.A., 2001. Chemostratigraphy of the Paleoproterozoic Duitschland Formation,
797 South Africa: Implications for coupled climate change and carbon cycling. American
798 Journal of Science 301, 261-285.
799 Bekker, A., Krapež, B., Karhu, J.A., 2002. Preliminary chemostratigraphic data on
800 carbonates from the Paleoproterozoic Turee Creek Supersequence and Wooly Dolomite
801 of Western Australia. 16th International Sedimentologic Congress Abstract Volume, 26-
802 27.
803 Bekker, A., Sial, A.N., Karhu, J.A., Ferreira, V.P., Noce, C.M., Kaufman, A.J., Romano,
804 A.W., Pimentel, M.M., 2003b. Chemostratigraphy of carbonates from the Minas
805 Supergroup, Quadrilátero Ferrifero, Brazil: A stratigraphic record of early Proterozoic
806 atmospheric, biogeochemical and climatic change. American Journal of Science 303,
807 865-904.
808 Bergmann, K.D., Grotzinger, J.P., Fischer, W.W., 2013. Biological influences on seafloor
809 carbonate precipitation. Palaios 28, 99-115.
810 Blake, T.S., Barley, M.E., 1992. Tectonic evolution of the late Archaean to early
811 Proterozoic Mount Bruce mega sequence set, Western Australia. Tectonics 11, 1415–
812 1425.

Bosak, T., Bush, J., Flynn, M., Liang, B., Ono, S., Petroff, A.P., Sim, M.S., 2010. Formation and stability of oxygen-rich bubbles that shape photosynthetic mats. Geobiology 8, 45–55.

Bosak, T., Liang, B., Sim, M.S., Petroff, A.P., 2009. Morphological record of oxygenic photosynthesis in conical stromatolites. Proceedings of the National Academy of Sciences 106, 10939–10943.

Brasier, A.T., Martin, A.P., Melezhik, V.A., Prave, A.R., Condon, D.J., Fallick, A.E., 2013. Earth's earliest global glaciation? Carbonate geochemistry and geochronology of the Polisarka Sedimentary Formation, Kola Peninsula, Russia. Precambrian Research 235, 278-294.

Canfield, D.E., 2014. Oxygen: A Four Billion Year History. Princeton University Press, Princeton, New Jersey.

Canfield, D.E., Ngombi-Pemba, L., Hammarlund, E.U., Bengtson, S., Chaussidon, M., Gauthier-Lafaye, F., Meunier, A., Riboulleau, A., Rollion-Bard, C., Rouxel, O., Asael, D., Pierson-Wickmann, A.-C., El Albani, A., 2013. Oxygen dynamics in the aftermath of the Great Oxidation of Earth's atmosphere. Proceedings of the National Academy of Sciences 110, 16736-16741.

Farquhar, J., Bao, H., Thiemens, M., 2000. Atmospheric influence of Earth's earliest sulfur cycle. Science 289, 756–758.

Flannery, D.T., Walter, M.R., 2012. Archean tufted microbial mats and the Great Oxidation Event: new insights into an ancient problem. Australian Journal of Earth Sciences 59, 1-11.

835 Fralick, P.W., Poulton, S.W., Canfield, D.E., 2011. Does the Paleoproterozoic Animikie
836 Basin record the sulfidic ocean transition?: COMMENT. Geology 39, e241.
837 Grotzinger, J.P., Knoll, A.H., 1999. Stromatolites in Precambrian carbonates:
838 Evolutionary mileposts or environmental dipsticks? Annual Review of Earth and
839 Planetary Sciences 27, 313-358.
840 Halverson, G.P., Shields-Zhou, G., 2011. Chapter 4 Chemostratigraphy and the
841 Neoproterozoic glaciations. Geological Society, London, Memoirs 36, 51-66.
842 Hannah, J.L., Bekker, A., Stein, H.J., Markey, R.J., Holland, H.D., 2004. Primitive Os
843 and 2316 Ma age for marine shale: implications for Paleoproterozoic glacial events and
844 the rise of atmospheric oxygen. Earth and Planetary Science Letters 225, 43-52.
845 Hoffman, P.F., 2013. The Great Oxidation and a Siderian snowball Earth: MIF-S based
846 correlation of Paleoproterozoic glacial epochs. Chemical Geology 362, 143-156.
847 Hofmann, H.J., Masson, M., 1994. Archean stromatolites from the Abitibi greenstone
848 belt, Quebec, Canada. Geological Society of America Bulletin 106, 424-429.
849 Horwitz, R.C., 1982. Geological history of the Early Proterozoic Paraburdoo Hinge Zone,
850 Western Australia. Precambrian Research 19, 191-200.
851 Hotinski, R.M., Kump, L.R., Arthur, M.A., 2004. The effectiveness of the
852 Paleoproterozoic biological pump: A $\delta^{13}C$ gradient from platform carbonates of the
853 Pethei Group (Great Slave Lake Supergroup, NWT). Geological Society of America
854 Bulletin 116, 539-554.
855 Irwin, H., Curtis, C., Coleman, M., 1977. Isotopic evidence for source of diagenetic
856 carbonates formed during burial of organic-rich sediments. Nature 269, 209-213.

857 Johnston, D.T., Macdonald, F.A., Gill, B.C., Hoffman, P.F., Schrag, D.P., 2012.
858 Uncovering the Neoproterozoic carbon cycle. Nature 483, 320-323.
859 Karhu, J.A., Holland, H.D., 1996. Carbon isotopes and the rise of atmospheric oxygen.
860 Geology 24, 867-870.
861 Kaufman, A.J., Hayes, J.M., Klein, C., 1990. Primary and diagenetic controls of isotopic
862 compositions of iron-formation carbonates. Geochimica et Cosmochimica Acta 54,
863 3461–3473.
864 Kirschvink, J.L., Gaidos, E.J., Bertani, L.E., Beukes, N.J., Gutzmer, J., Maepa, L.N.,
865 Steinberger, R.E., 2000. Paleoproterozoic snowball Earth: Extreme climatic and
866 geochemical global change and its biological consequences. Proceedings of the National
867 Academy of Sciences, U.S.A. 97, 1400–1405.
868 Knoll, A.H., Beukes, N.J., 2009. Introduction: Initial investigations of a Neoarchean shelf
869 margin-basin transition (Transvaal Supergroup, South Africa). Precambrian Research
870 169, 1-14.
871 Knoll, A.H., Wörndle, S., Kah, L.C., 2013. Covariance of microfossil assemblages and
872 microbialite textures across an upper Mesoproterozoic carbonate platform. Palaios 28,
873 453-470.
874 Konhauser, K.O., Lalonde, S.V., Planavsky, N.J., Pecoits, E., Lyons, T.W., Mojzsis, S.J.,
875 Rouxel, O.J., Barley, M.E., Rosiere, C., Fralick, P.W., Kump, L.R., Bekker, A., 2011.
876 Aerobic bacterial pyrite oxidation and acid rock drainage during the Great Oxidation
877 Event. Nature 478, 369-373.
878 Konhauser, K.O., Urrutia, M.M., 1999. Bacterial clay authigenesis: a common
879 biogeochemical process. Chemical Geology 161, 399-413.

880 Krapež, B., 1996. Sequence stratigraphic concepts applied to the identification of basin-
881 filling rhythms in Precambrian successions. Australian Journal of Earth Sciences 43,
882 355–380.
883 Kump, L.R., Junium, C., Arthur, M.A., Brasier, A., Fallick, A., Melezhik, V., Lepland,
884 A., Črne, A.E., Luo, G., 2011. Isotopic evidence for massive oxidation of organic matter
885 following the Great Oxidation Event. Science 334, 1694-1696.
886 Lepot, K., Benzerara, K., Brown, G.E., Phillipot, P., 2008. Microbially influenced
887 formation of 2,724-million-year-old stromatolites. Nature Geoscience 1, 118 - 121.
888 Lepot, K., Benzerara, K., Rividi, N., Cotte, M., Brown Jr, G.E., Philippot, P., 2009.
889 Organic matter heterogeneities in 2.72 Ga stromatolites: Alteration versus preservation
890 by sulfur incorporation. Geochimica et Cosmochimica Acta 73, 6579-6599.
891 Léveillé, R.J., Fyfe, W.S., Longstaffe, F.J., 2000. Geomicrobiology of carbonate–silicate
892 microbialites from Hawaiian basaltic sea caves. Chemical Geology 169, 339-355.
893 Lindsay, J.F., Brasier, M.D., 2002. Did global tectonics drive early biosphere evolution?
894 Carbon isotope record from 2.6 to 1.9 Ga carbonates of Western Australian basins.
895 Precambrian Research 114, 1-34.
896 Lyons, T.W., Reinhard, C.T., Love, G., Xiao, S., 2012. Geobiology of the Proterozoic
897 Eon, in: Knoll, A.H., Canfield, D.E., and Konhauser, K.O. (Ed.), Fundamentals of
898 Geobiology. Blackwell, pp. 371-402.
899 Lyons, T.W., Reinhard, C.T., Planavsky, N.J., 2014. The rise of oxygen in Earth's early
900 ocean and atmosphere. Nature 506, 307-315.
901 Maheshwari, A., Sial, A.N., Gaucher, C., Bossi, J., Bekker, A., Ferreira, V.P., Romano,
902 A.W., 2010. Global nature of the Paleoproterozoic Lomagundi carbon isotope excursion:

903 A review of occurrences in Brazil, India, and Uruguay. Precambrian Research 182, 274-
904 299.
905 Martin, A.P., Condon, D.J., Prave, A.R., Lepland, A., 2013. A review of temporal
906 constraints for the Palaeoproterozoic large, positive carbonate carbon isotope excursion
907 (the Lomagundi–Jatuli Event). Earth-Science Reviews 127, 242-261.
908 Martin, D.M., 1999. Depositional setting and implications of Paleoproterozoic
909 glaciomarine sedimentation in the Hamersley Province, Western Australia. Geological
910 Society of America Bulletin 111, 189-203.
911 Martin, D.M., Li, Z.X., Nemchin, A.A., Powell, C.M., 1998. A pre-2.2 Ga age for giant
912 hematite ores of the Hamersley Province Australia? . Economic Geology 93, 1084–1090.
913 Martin, D.M., Powell, C.M., George, A.D., 2000. Stratigraphic architecture and evolution
914 of the early Paleoproterozoic McGrath Trough, Western Australia. Precambrian Research
915 99, 33-64.
916 Mata, S.A., Harwood, C.L., Corsetti, F.A., Stork, N.J., Eilers, K., Berelson, W.M., Spear,
917 J., 2012. Influences of gas production and filament orientation on stromatolite
918 microfabric. Palaios 27, 206-219.
919 Mazumder, R., Van Kranendonk, M.J., Altermann, W., 2015. A marine to fluvial
920 transition in the Paleoproterozoic Koolbye Formation, Turee Creek Group, Western
921 Australia. Precambrian Research 258, 161–170.
922 McLoughlin, N.J., Melezhik, V.A., Brasier, A.T., Medvedev, P.V., 2013.
923 Palaeoproterozoic stromatolites from the Lomagundi-Jatuli interval of the Fennoscandian
924 Shield., in: A. Prave, A.E.F., V.A. Melezhik, A. Lepland, E.J. Hanski, & H. Strauss (Ed.),
925 Reading the archive of Earth's oxygenation: Global events and the Fennoscandian Arctic

926 Russia - Drilling Early Earth Project (FAR-DEEP) (Frontiers in Earth Sciences, 3).
927 Springer, Heidelberg, pp. 1298-1351.
928 Medvedev, P., Bekker, A., Karhu, J.A., Kortelainen, N., 2005. Testing the
929 biostratigraphic potential of early Paleoproterozoic microdigitate stromatolites. Revista
930 Española de Micropaleontologia 37, 41-56.
931 Melezhik, V.A., Fallick, A.E., 2010. On the Lomagundi-Jatuli carbon isotopic event: The
932 evidence from the Kalix Greenstone Belt, Sweden. Precambrian Research 179, 165-190.
933 Mohanty, S.P., Barik, A., Sarangi, S., Sarkar, A., 2015. Carbon and oxygen isotope
934 systematics of a Paleoproterozoic cap-carbonate sequence from the Sausar Group,
935 Central India. Palaeogeography, Palaeoclimatology, Palaeoecology 417, 195-209.
936 Müller, S.G., Krapež, B., Barley, M.E., Fletcher, I.R., 2005. Giant iron-ore deposits of
937 the Hamersley province related to the breakup of Paleoproterozoic Australia: New
938 insights from in situ SHRIMP dating of baddeleyite from mafic intrusions. Geology 33,
939 577-580.
940 Partin, C.A., Lalonde, S.V., Planavsky, N.J., Bekker, A., Rouxel, O.J., Lyons, T.W.,
941 Konhauser, K.O., 2013. Uranium in iron formations and the rise of atmospheric oxygen.
942 Chemical Geology 362, 82-90.
943 Planavsky, N.J., Asael, D., Hofmann, A., Reinhard, C.T., Lalonde, S.V., Knudsen, A.,
944 Wang, X., Ossa, F.O., Pecoits, E., Smith, A.J.B., Beukes, N.J., Bekker, A., Johnson,
945 T.M., Konhauser, K.O., Lyons, T.W., Rouxel, O.J., 2014. Evidence for oxygenic
946 photosynthesis half a billion years before the Great Oxidation Event. Nature Geoscience
947 7, 283-286.

948 Planavsky, N.J., Bekker, A., Hofmann, A., Owens, J.D., Lyons, T.W., 2012. Sulfur
949 record of rising and falling marine oxygen and sulfate levels during the Lomagundi event.
950 Proceedings of the National Academy of Sciences 109, 18300-18305.
951 Powell, C.M., Horwitz, R.C., 1994. Late Archaean and early Proterozoic tectonics and
952 basin formation of the Hamersley Ranges, Twelfth Australian Geological Convention,
953 Perth, Geological Society of Australia (WA Division), Excursion Guidebook, 4, p. 53.
954 Pufahl, P.K., Hiatt, E.E., 2012. Oxygenation of the Earth's ocean-atmosphere system: a
955 review of physical and chemical sedimentological responses. Marine and Petroleum
956 Geology 32, 1-20.
957 Pufahl, P.K., Hiatt, E.E., Kyser, T.K., 2010. Does the Paleoproterozoic Animikie Basin
958 record the sulfidic ocean transition? Geology 38, 659-662.
959 Pufahl, P.K., Hiatt, E.E., Kyser, T.K., 2011. Does the Paleoproterozoic Animikie Basin
960 record the sulfidic ocean transition? REPLY. Geology 39, e242-e243.
961 Rasmussen, B., Bekker, A., Fletcher, I.R., 2013. Correlation of Paleoproterozoic
962 glaciations based on U–Pb zircon ages for tuff beds in the Transvaal and Huronian
963 Supergroups. Earth and Planetary Science Letters 382, 173-180.
964 Reinhard, C.T., Planavsky, N.J., Robbins, L.J., Partin, C.A., Gill, B.C., Lalonde, S.V.,
965 Bekker, A., Konhauser, K.O., Lyons, T.W., 2013. Proterozoic ocean redox and
966 biogeochemical stasis. Proceedings of the National Academy of Sciences 110, 5357-
967 5362.
968 Riding, R., Fralick, P., Liang, L., 2014. Identification of an Archean marine oxygen oasis.
969 Precambrian Research 251, 232-237.

970 Scott, C., Wing, B.A., Bekker, A., Planavsky, N.J., Medvedev, P., Bates, S.M., Yun, M.,
971 Lyons, T.W., 2014. Pyrite multiple-sulfur isotope evidence for rapid expansion and
972 contraction of the early Paleoproterozoic seawater sulfate reservoir. Earth and Planetary
973 Science Letters 389, 95-104.
974 Sumner, D.Y., 1997. Late Archean calcite-microbe interactions: Two morphologically
975 distinct microbial communities that affected calcite nucleation differently. Palaios 12,
976 302-318.
977 Swanner, E.D., Planavsky, N.J., Lalonde, S.V., Robbins, L.J., Bekker, A., Rouxel, O.J.,
978 Saito, M.A., Kappler, A., Mojzsis, S.J., Konhauser, K.O., 2014. Cobalt and marine redox
979 evolution. Earth and Planetary Science Letters 390, 253-263.
980 Takehara, M., Komure, M., Kiyokawa, S., Horie, K., Yokohama, K., 2010. Detrital
981 zircon SHRIMP U–Pb age of the 2.3Ga diamictites of the Meteorite Bore Member in the
982 South Pilbara, Western Australia., in: Tyler, I.M., Knox-Robinson, C.M. (Eds.), Fifth
983 International Archean Symposium Abstracts: Geological Survey of Western Australia,
984 Record 2010/18, pp. 223–222.
985 Thorne, A.M., 1990. Ashburton Basin, in Geology and Mineral Resources of Western
986 Australia: Geological Survey of Western Australia, Memoir 3, 210-219.
987 Thorne, A.M., Seymour, D.B., 1991. Geology of the Ashburton Basin Western Australia:
988 Geological Survey of Western Australia, Bulletin 139.
989 Thorne, A.M., Tyler, I.M., 1996. Roy Hill, Western Australia Sheet 50-12: Geological
990 Survey of Western Australia, 1:250 000 map series.
991 Thorne, A.M., Tyler, I.M., Blight, D.F., 1995. Rocklea, Western Australia: Geological
992 Survey of Western Australia, 1:100 000 geological series.

993 Trendall, A.F., 1969. Three great basins of Precambrian banded iron formation
994 deposition: A systematic comparison. Geological Society of America Bulletin 79, 1527-
995 1544.
996 Trendall, A.F., 1976. Striated and faceted boulders from the Turee Creek Formation –
997 Evidence for a possible Huronian glaciation on the Australian continent, Geological
998 Survey of Western Australia Annual Report 1975, pp. 88-92.
999 Trendall, A.F., 1979. A revision of the Mount Bruce Supergroup. Geological Survey of
1000 Western Australia Annual Report 1978, 63–71.
1001 Trendall, A.F., 1981. The Lower Proterozoic Meteorite Bore Member, Hamersley Basin,
1002 Western Australia, in: Hambrey, M.J., Harland, W.B. (Eds.), Earth's Pre-Pleistocene
1003 glacial record. Cambridge University Press, Cambridge, pp. 555–557.
1004 Trendall, A.F., 1990. Hamersley Basin, in Geology and Mineral Resources of Western
1005 Australia. Geological Survey of Western Australia, Memoir 3, 163-190.
1006 Trendall, A.F., Blockley, J.G., 1970. The iron formations of the Precambrian Hamersley
1007 Group, Western Australia with special reference to the crocidolite. Geological Survey of
1008 Western Australia, Bulletin 119, 1-366.
1009 Trendall, A.F., Trendall, A.F., Morris, R.C., 1983. Chapter 3 The Hamersley Basin,
1010 Developments in Precambrian Geology. Elsevier, pp. 69-129.
1011 Tyler, I.M., Thorne, A.M., 1990. The northern margin of the Capricorn Orogen, Western
1012 Australia—an example of an Early Proterozoic collision zone. Journal of Structural
1013 Geology 12, 685-701.
1014 Van Kranendonk, M., 2010. Three and a half billion years of life on Earth: A transect
1015 back in time. Geological Survey of Western Australia Record 2010/21.

1016 Van Kranendonk, M.J., Altermann, W., Beard, B.L., Hoffman, P.F., Johnson, C.J.,
1017 Kasting, J.F., Melezhik, V.A., Nutman, A.P., Papineau, D., Pirajno, F., 2012. A
1018 chronostratigraphic division of the Precambrian: possibilities and challenges, in:
1019 Gradstein, F.M., Ogg, J.G., Schmitz, M.D., Ogg, G.J. (Eds.), The Geologic Time Scale
1020 2012. Elsevier, Boston, USA, pp. 299–392.
1021 Van Kranendonk, M.J., Mazumder, R., 2015. Two Paleoproterozoic glacio-eustatic
1022 cycles in the Turee Creek Group, Western Australia. Geological Society of America
1023 Bulletin 127, 596-607.
1024 Van Kranendonk, M.J., Mazumder, R., Yamaguchi, K.E., Yamada, K., Ikehara, M.,
1025 2015. Sedimentology of the Paleoproterozoic Kungarra Formation, Turee Creek Group,
1026 Western Australia: A conformable record of the transition from early to modern Earth.
1027 Precambrian Research 256, 314-343.
1028 Williford, K.H., Van Kranendonk, M.J., Ushikubo, T., Kozdon, R., Valley, J.W., 2011.
1029 Constraining atmospheric oxygen and seawater sulfate concentrations during
1030 Paleoproterozoic glaciation: In situ sulfur three-isotope microanalysis of pyrite from the
1031 Turee Creek Group, Western Australia. Geochimica et Cosmochimica Acta 75, 5686-
1032 5705.

1033

1034

Figure captions

Figure 1. Geographic, stratigraphic, and geological location of the studied sections. Upper left: Location of study area in Australia (star). Upper right: stratigraphic context for the Turee Creek Group; stars indicate stratigraphic horizons of studied sections. Bottom: Geological map of the Hardey Syncline from Martin et al. (2000); numbered circles indicate studied localities.

Figure 2. Litho- and chemostratigraphy of the Kungarra Formation section at Horseshoe Creek (composite section of stratigraphic columns HC1, HC2, and HC3). The stratigraphic interval between 33.9 m and 34.4 m has been enlarged to show the succession of stromatolitic textures (interpreted to be of microbial origin). Inset images are photomicrographs (plane polarized light) of the Kungarra carbonates; sample HC2 12.5A is from 13.8 m and HC3 40.2 is from 40.2 m. Dots in inset images indicate microsampling locations and their carbon isotope values.

Figure 3. Kungarra Formation carbonates at Horseshoe Creek. A) Pinkish-white micritic limestone interbedded with reddish-brown fine-grained sandstone forming starved ripples, Australian dollar for scale (25 mm diameter). B) Close up of stromatolites from roughly 34.2 m in stratigraphic height, Australian dollar for scale. C) Petrographic view of the domal stromatolite layer (Sample HC3 34.3, 34.3m in stratigraphic height), showing overgrowths of calcite on micritic carbonates stained by iron oxides (note scale bar).

1058 Figure 4. Elemental map of Kungarra Formation limestone (sample HC3 16.25 from
1059 16.25m in stratigraphic height); top images are the entire sample, and the bottom images
1060 are close up views of the boxed area. On the left are SEM images, on the right are false
1061 color representations of the elemental maps, and the middle images are a composite
1062 image of the SEM images and elemental maps. Note that the calcium (calcite) only
1063 manifests in rare lenses with abundant detrital minerals, suggesting that it is not primary
1064 carbonate but rather diagenetic.
1065
1066 Figure 5. Lithologies of the Kazput Formation in Hardey Syncline section K1. A)
1067 Overview of stratigraphy, section K1 begins in the thin-bedded limestones in the
1068 foreground, the base of the cliff is at 53 m elevation in the stratigraphic column (Fig. 6),
1069 and the measured section continues up the gully on the left. B) Close-up of thin-bedded
1070 limestones at the base of the K1 section, hammer for scale. C) Cross-stratified
1071 grainstones with abundant bed-parallel silicification at meter 108 in the K1 section,
1072 Sharpie tip for scale.
1073
1074 Figure 6. Litho- and chemostratigraphy of the Kazput Formation at section K1.
1075
1076 Figure 7. Lithologies of the Kazput Formation in Hardey Syncline section K2. A)
1077 Overview of stratigraphy, showing where individual subsections were measured. B) Fine
1078 grained, parallel-laminated facies in section K2A, Australian dollar for scale (25 mm
1079 diameter). C) Section K2B; silty to (fine) sandy carbonates with small-scale ripples in the
1080 lower half of the photo and mm-scale laminations in the upper half. Blue ruler at the

bottom of the photo is 10.5 cm long. D) Interbedded sandy carbonates and fine-grained carbonates with wavy to stromatolitic laminae (section K2B); rock hammer for scale.

Figure 8. Litho- and chemostratigraphy of the Kazput Formation at sections K2A and K2A2. Note that K2A2 sits stratigraphically above the K2A section.

Figure 9. Litho- and chemostratigraphy of Kazput Formation at sections K2B and K2C. Expanded section in upper right highlights geochemical results from stromatolite microsampling.

Figure 10. Kazput stromatolites. A) Large domal stromatolites forming over relict topography at 47 m stratigraphic height (in section K2C). B) Thin stromatolite layer within fine-grained micritic limestones; note the eroded base on which the stromatolite accreted. C) Alternating layers of siliciclastic lamina-rich (resistant) and carbonate-rich (recessive) layers within the larger stromatolites; note the weathering difference between units. D) Top layers of domal stromatolites from K2C (47 m), note the alternating layers of siliciclastic lamina-rich and carbonate-rich layers. The stromatolites on the top layer formed much larger (>5 cm), more cement-rich structures than earlier layers. E) Synsedimentary neptunian dyke through stromatolite layers, dark patches are shadows from vegetation on the outcrop. F) Domal stromatolites growing into microdigitate stromatolites within cement-rich intervals of the large domal stromatolites in K2C.

Figure 11. Petrographic textures of Kazput stromatolites (all plane polarized light). A) Alternating siliciclastic lamina-rich and discontinuous carbonate-rich layers of large domal stromatolites from section K2C (47 m, sample K2C 5.5B2); B) Unusually continuous carbonate-rich layers in section K2C (65.7 m, sample K2C 31.8m); C) Microstructure of a transported and rolled up stromatolite, showing the local preservation of fine banding in lenticular carbonate precipitates highlighted by arrows (63.4 m, sample K2C 28.6); D) Detail of a siliciclastic-rich lamina in a small stromatolite containing quartz, pyrite, and clay minerals, with carbonate-rich areas above and below (Sample K2C 28.5); E) Close up of Fig. 11C highlighting the faint banding within the carbonate fabric of the deformed stromatolite (63.4 m sample K2C 28.6).

Figure 12. Elemental map of Kazput Formation stromatolitic carbonates (sample KAZS1, 47 m height in section K2C); top row is an image of the entire sample, and the middle and bottom rows are close up views of boxes 1 and 2 respectively. Left column are SEM images, right column images are false color representations of the elemental maps, and the middle illustrations are composite images of the elemental and SEM maps. Note, unlike the Kungarra Fm. (Fig. 4), calcium (calcite) is the dominant mineral with quartz and aluminosilicates occurring with high relative abundance in stromatolitic laminae. Small iron oxide grains (blue in false color maps) occur throughout the Kazput section but are concentrated in silicate-rich laminae (orange in false color maps). There are also organic carbon inclusions throughout the section (see second row); they appear as black spots in the composite figure and are highlighted in red on the carbon (C) elemental map.

Figure 1

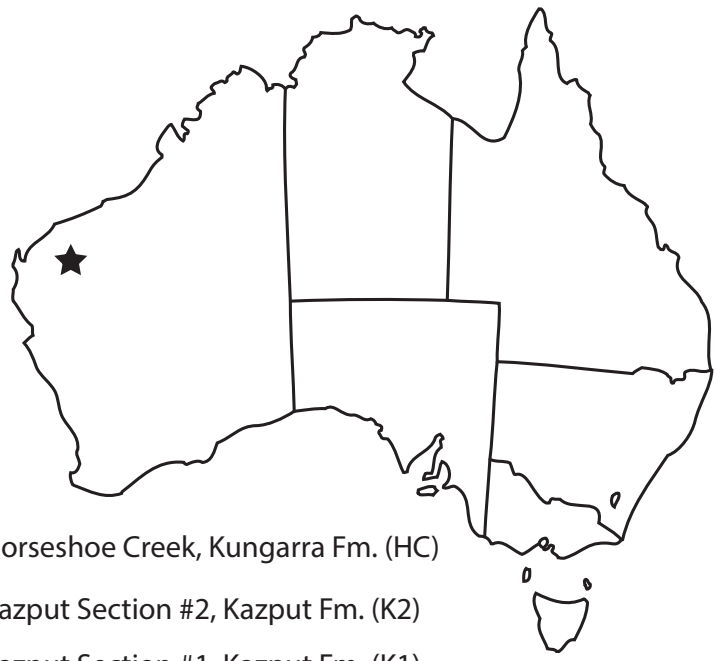

① Horseshoe Creek, Kungarra Fm. (HC)

② Kazput Section #2, Kazput Fm. (K2)

③ Kazput Section #1, Kazput Fm. (K1)

Wyloo Group	Mount McGrath Formation
	Cheela Springs Basalt (2209 ± 15 Ma)
	Beasley River Quartzite
Turee Creek Group	Kazput Formation ★
	Koolbye Formation
	Kungarra Formation: Meterorite Bore Mb. ★
Hamersley Group	Boolgeda Iron Formation
	Woongarra Rhyolite (2449 ± 3 Ma)
	Weeli Wolli Formation

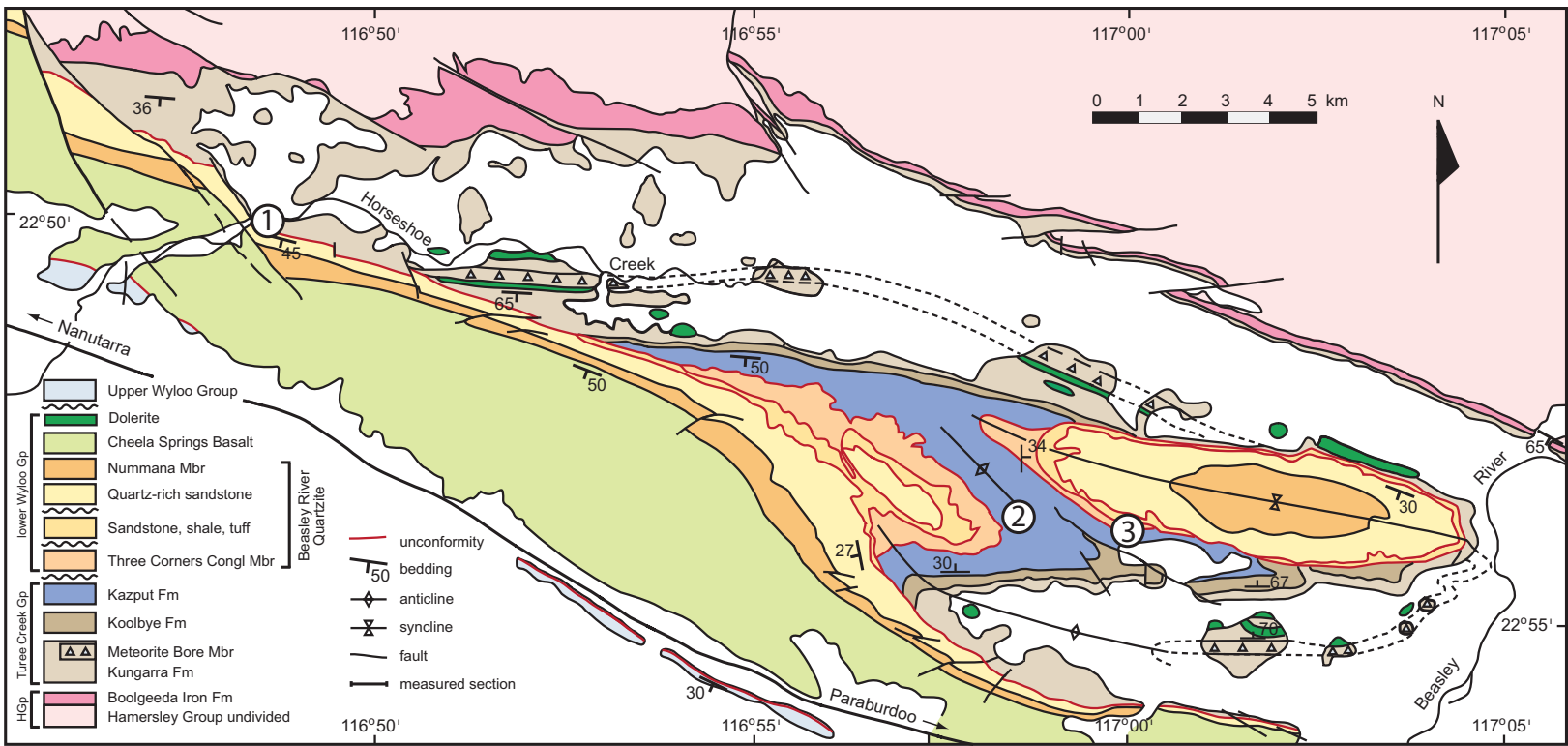

Figure 2

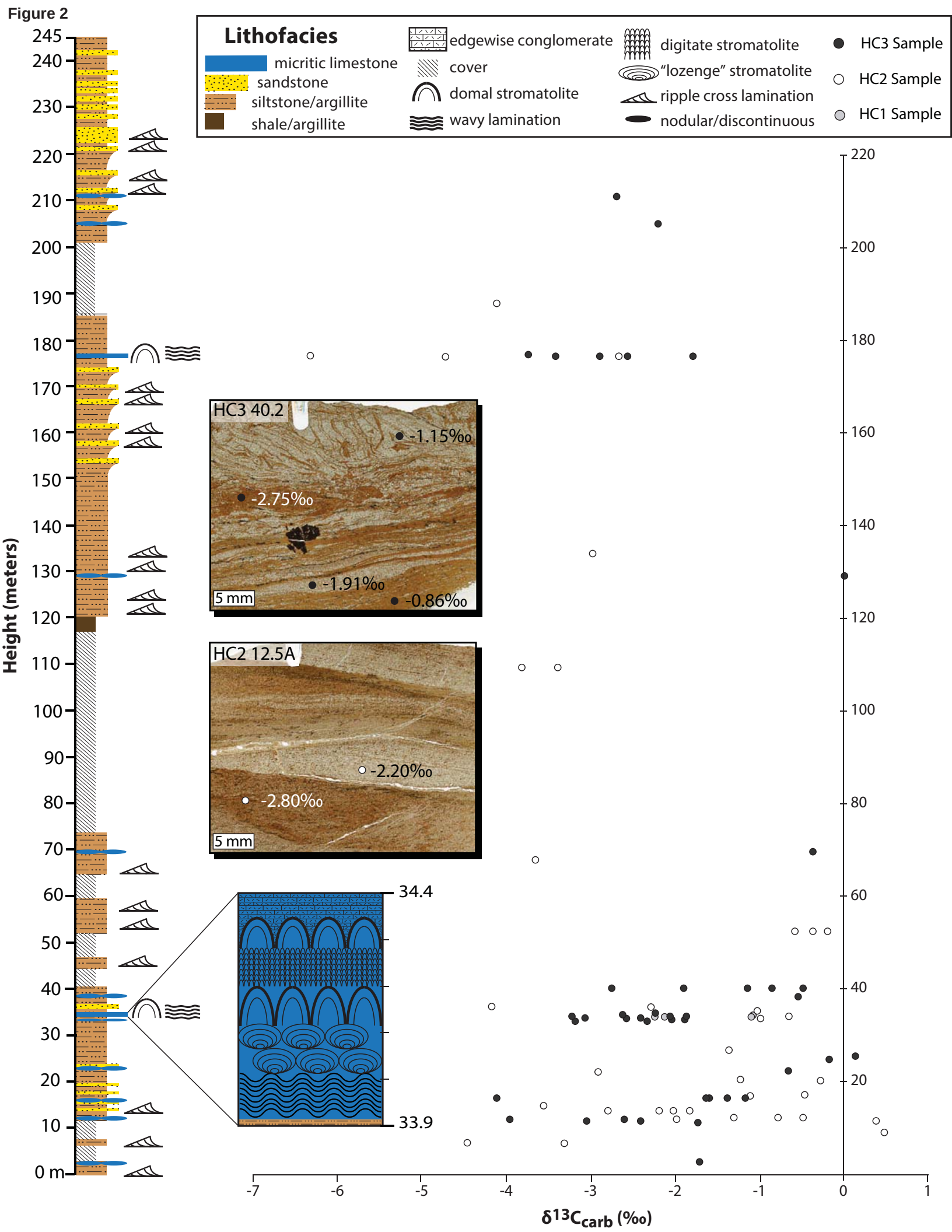
Lithofacies
micritic limestone
sandstone
siltstone/argillite
shale/argillite
edgewise conglomerate
cover
domal stromatolite
wavy lamination
digitate stromatolite
"lozenge" stromatolite
ripple cross lamination
nodular/discontinuous
HC3 Sample
HC2 Sample
HC1 Sample
HC3 40.2
-1.15‰
-2.75‰
-1.91‰
-0.86‰
5 mm
HC2 12.5A
-2.20‰
-2.80‰
5 mm
34.4
33.9
Height (meters)
δ13Ccarb (‰)

Figure 3

Click here to download high resolution image

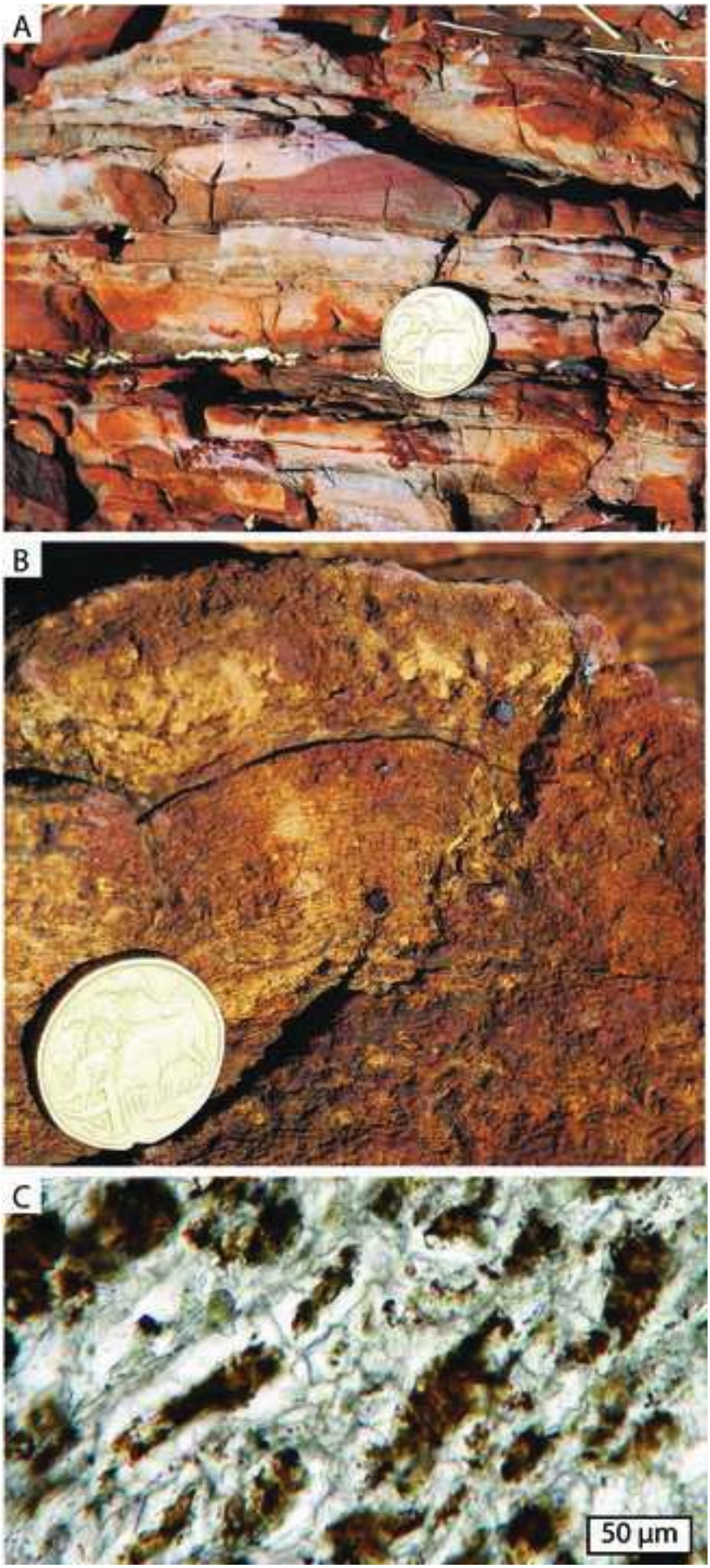

Figure 4

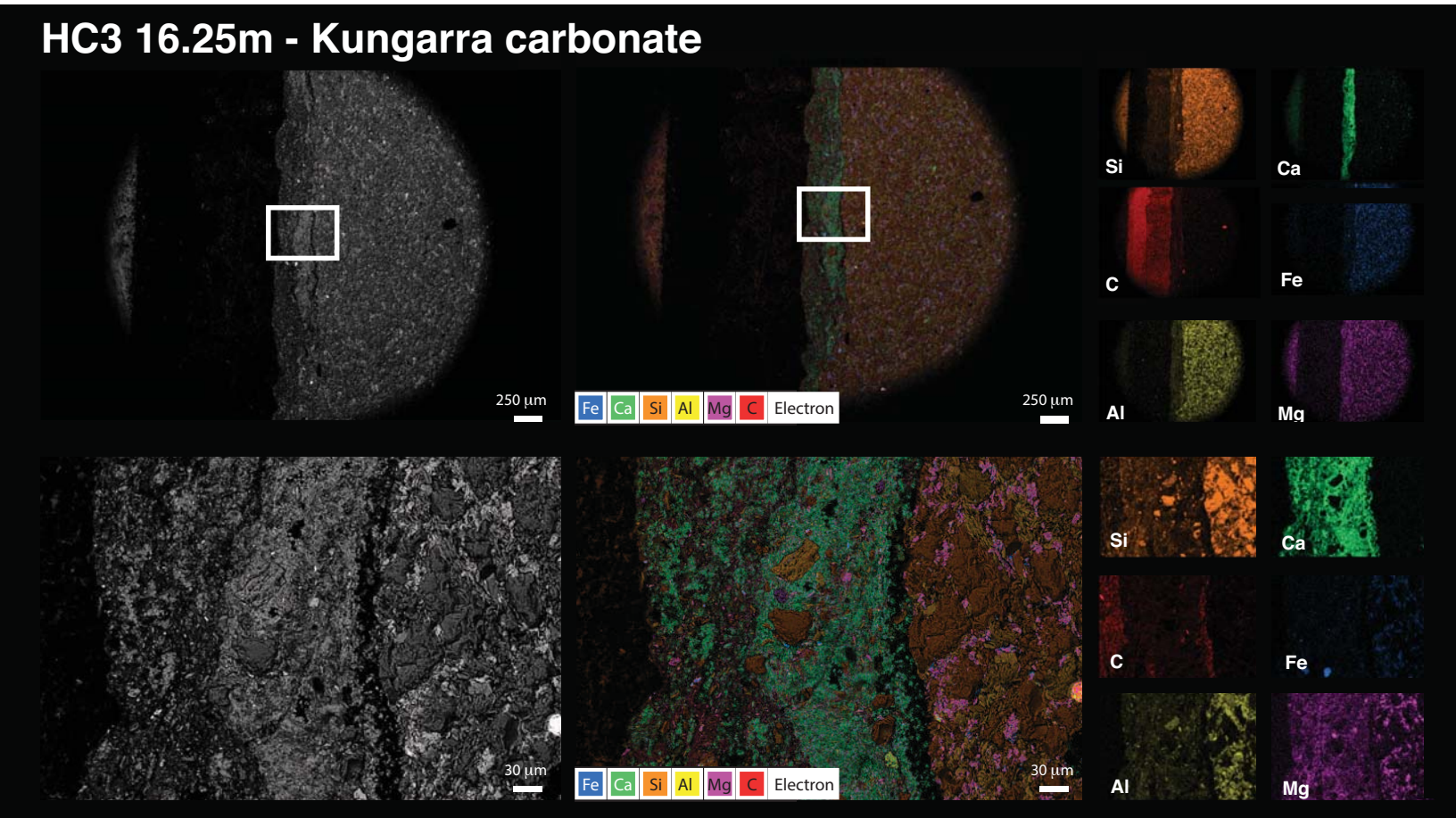
HC3 16.25m - Kungarra carbonate
250 µm
Fe Ca Si Al Mg C Electron
250 µm
Si
Ca
C
Fe
Al
Mg
30 µm
Fe Ca Si Al Mg C Electron
30 µm
Si
Ca
C
Fe
Al
Mg

Figure 5

Click here to download high resolution image

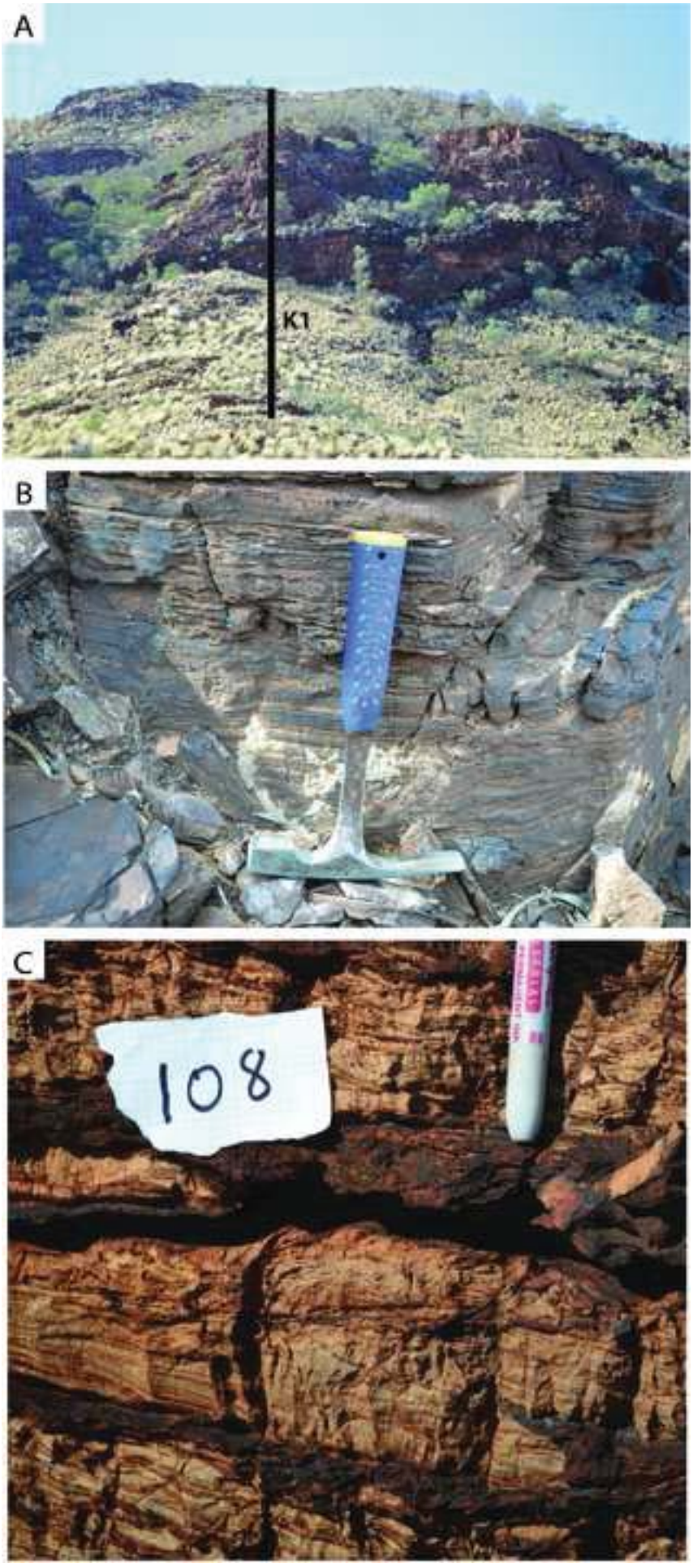

Figure 6

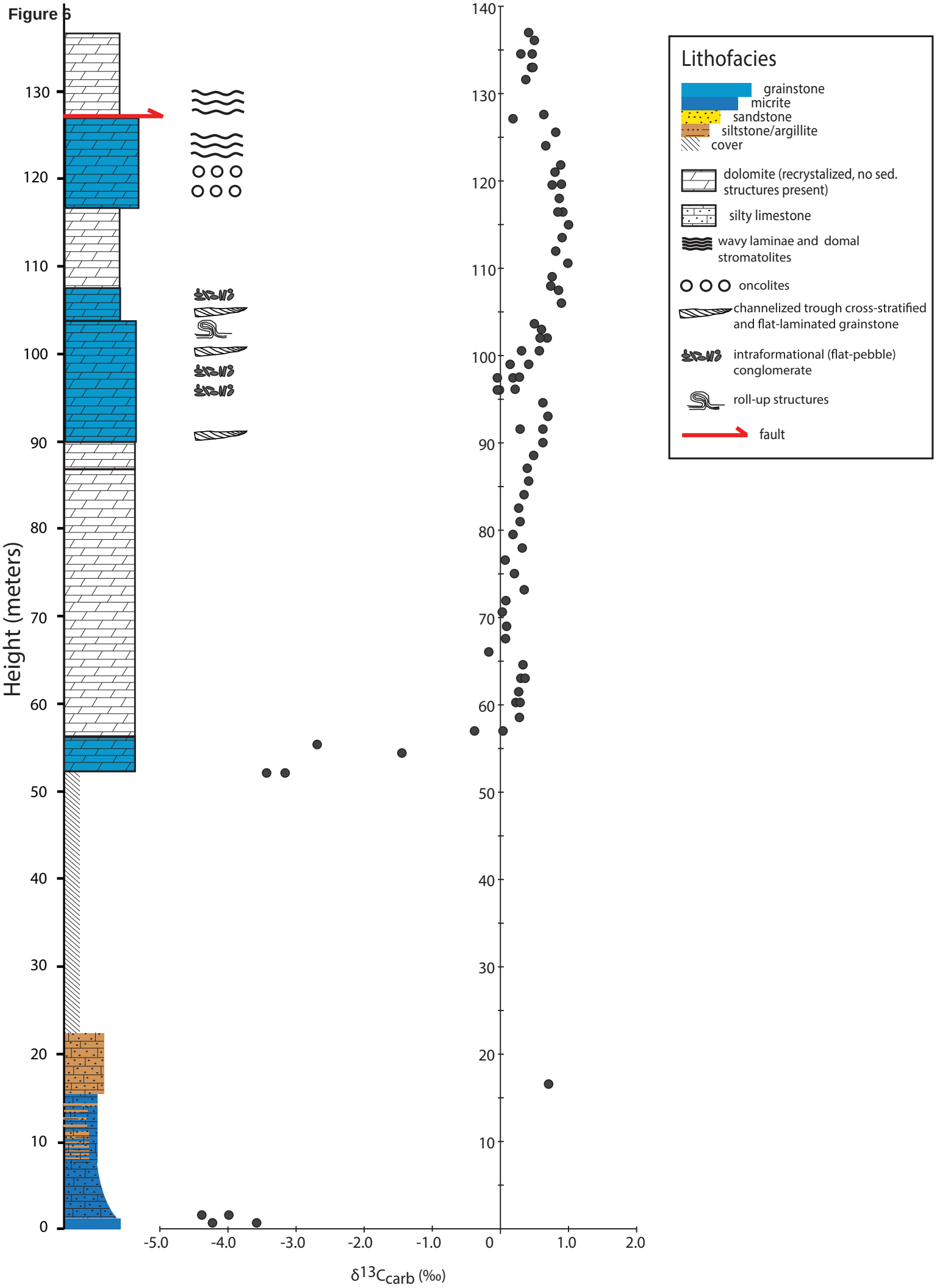
Lithofacies
grainstone
micrite
sandstone
siltstone/argillite
cover
dolomite (recrystalized, no sed. structures present)
silty limestone
wavy laminae and domal stromatolites
oncolites
channelized trough cross-stratified and flat-laminated grainstone
intraformational (flat-pebble) conglomerate
roll-up structures
fault
Height (meters)
0
10
20
30
40
50
60
70
80
90
100
110
120
130
140
-5.0
-4.0
-3.0
-2.0
-1.0
0
1.0
2.0
δ13Ccarb (‰)

Figure 7

Click here to download high resolution image

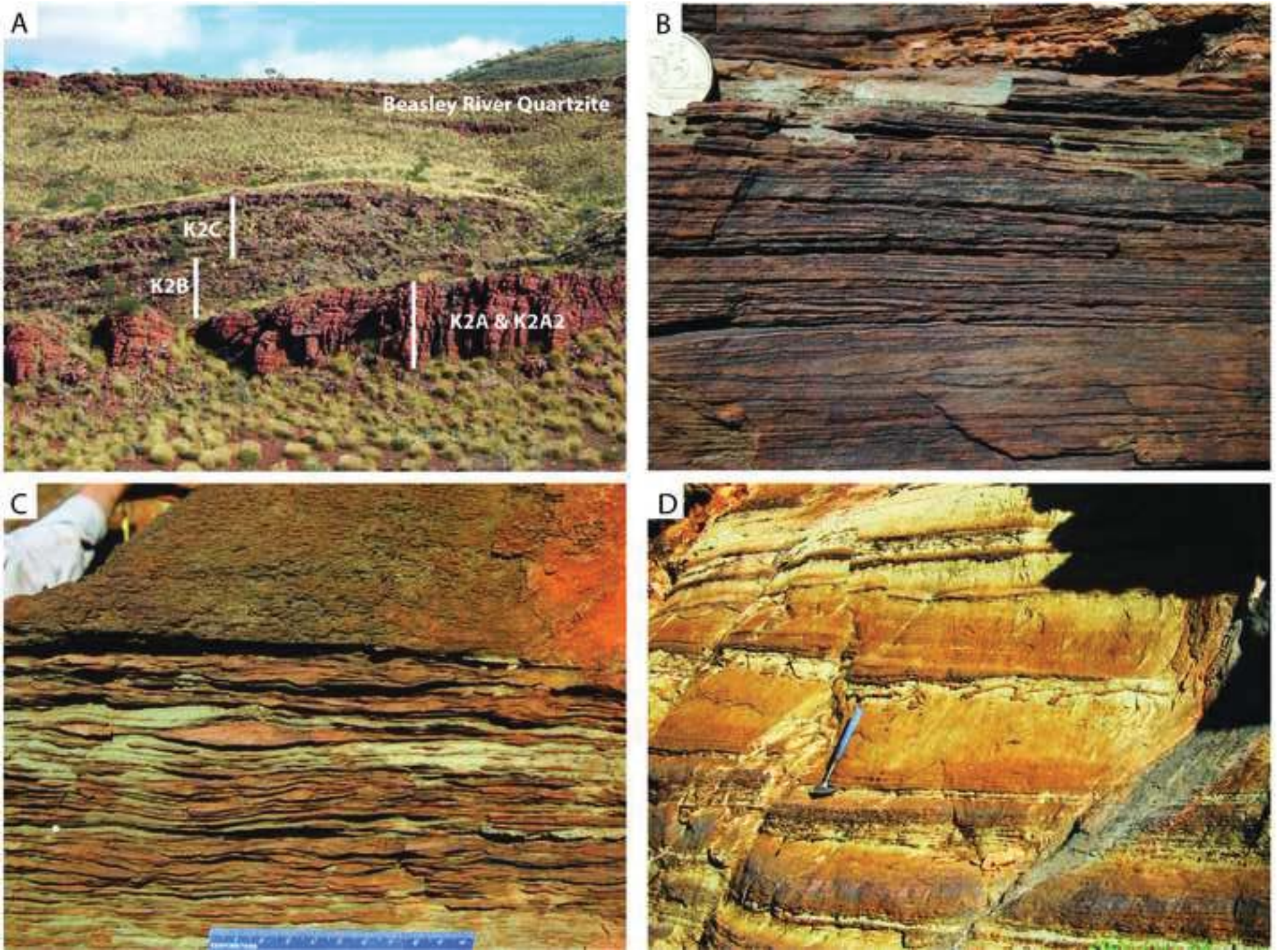

Figure 8

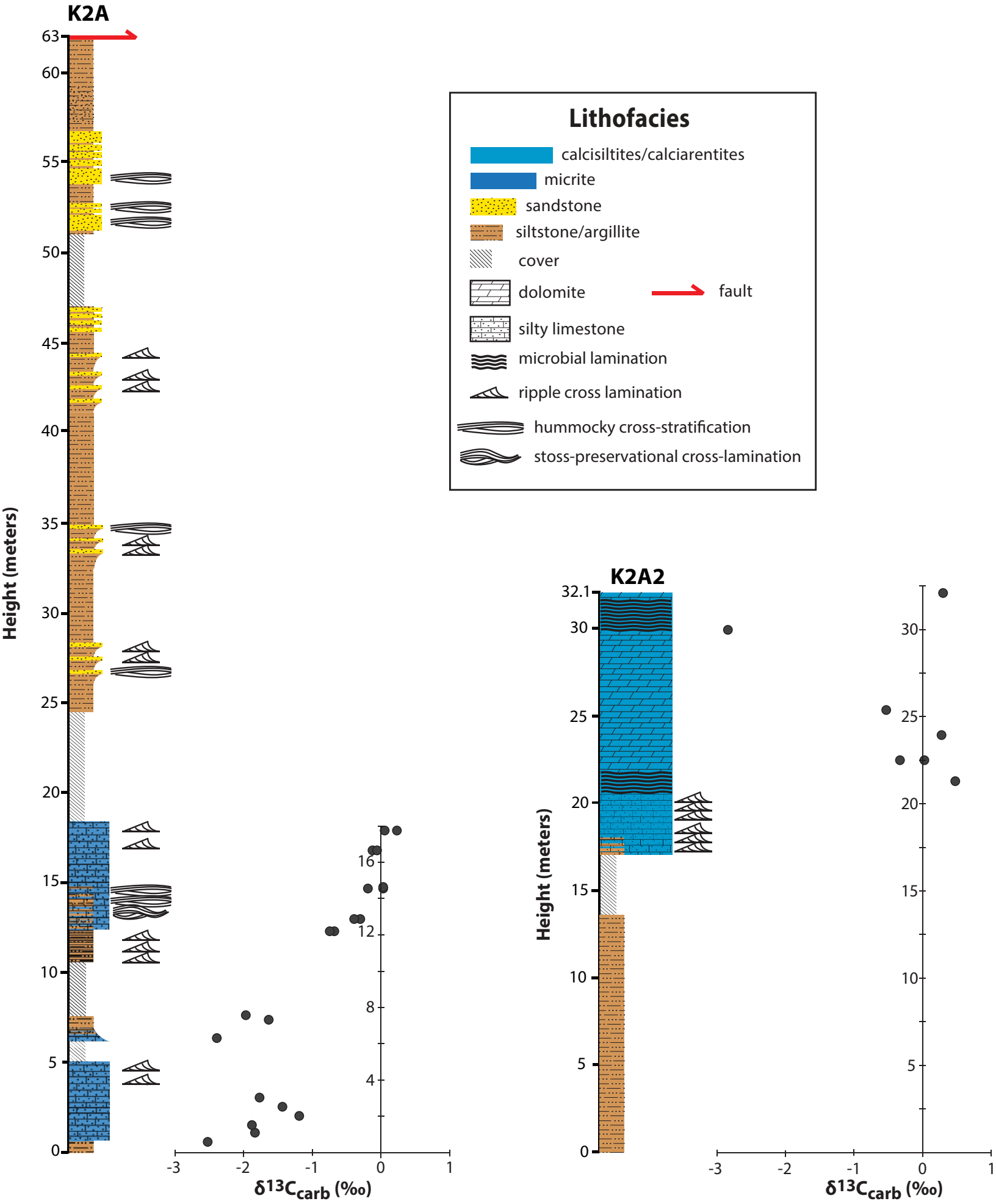
K2A
K2A2
Lithofacies
calcisiltites/calciarentites
micrite
sandstone
siltstone/argillite
cover
dolomite
fault
silty limestone
microbial lamination
ripple cross lamination
hummocky cross-stratification
stoss-preservational cross-lamination
Height (meters)
δ13Ccarb (‰)

Figure 9

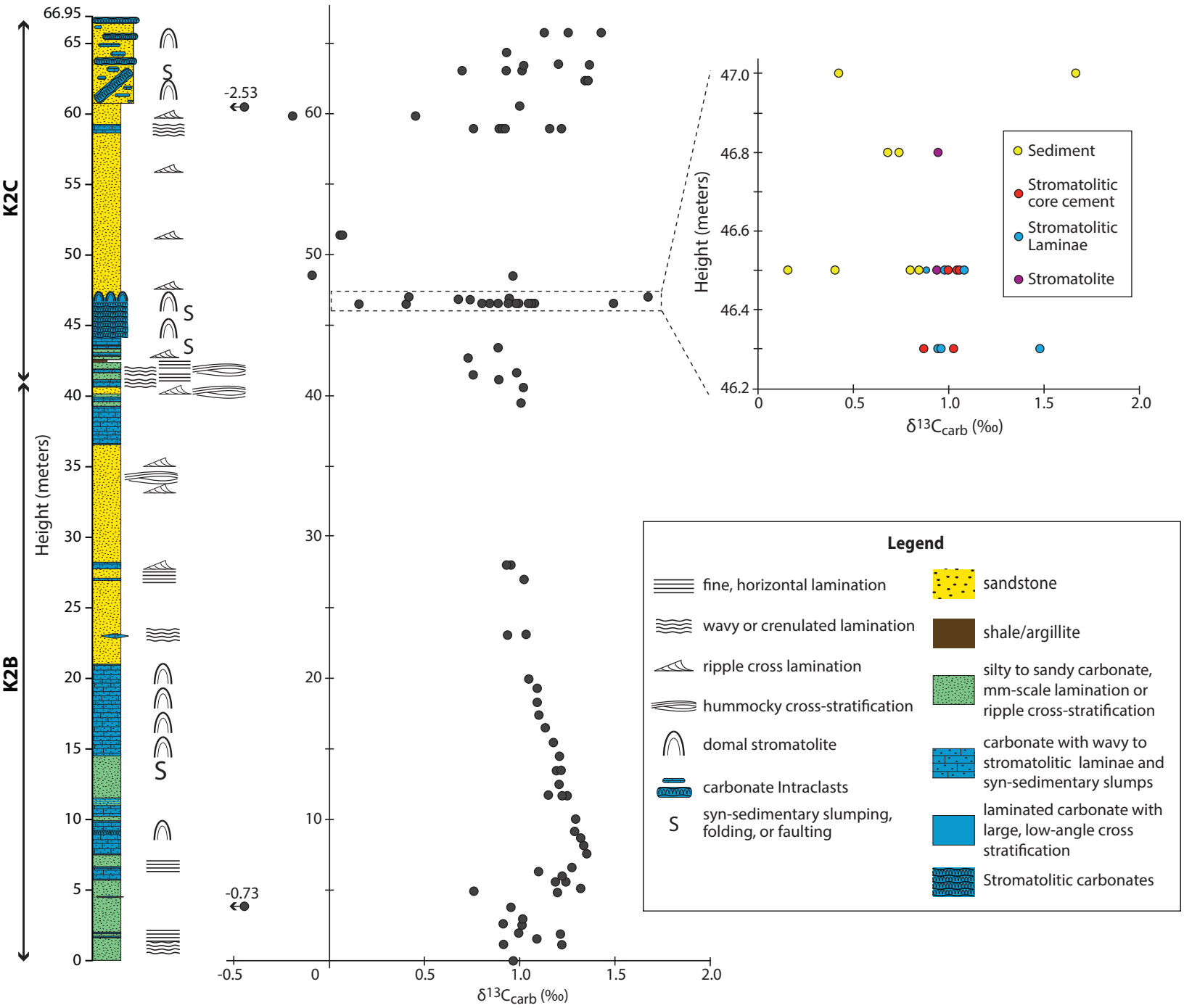
K2C
K2B
Height (meters)
66.95
65
60
55
50
45
40
35
30
25
20
15
10
5
0
S
-2.53
-0.73
-0.5
0
0.5
1.0
1.5
2.0
δ13Ccarb (‰)
47.0
46.8
46.6
46.4
46.2
Sediment
Stromatolitic core cement
Stromatolitic Laminae
Stromatolite
Legend
fine, horizontal lamination
wavy or crenulated lamination
ripple cross lamination
hummocky cross-stratification
domal stromatolite
carbonate Intraclasts
syn-sedimentary slumping, folding, or faulting
sandstone
shale/argillite
silty to sandy carbonate, mm-scale lamination or ripple cross-stratification
carbonate with wavy to stromatolitic laminae and syn-sedimentary slumps
laminated carbonate with large, low-angle cross stratification
Stromatolitic carbonates

Figure 10

Click here to download high resolution image

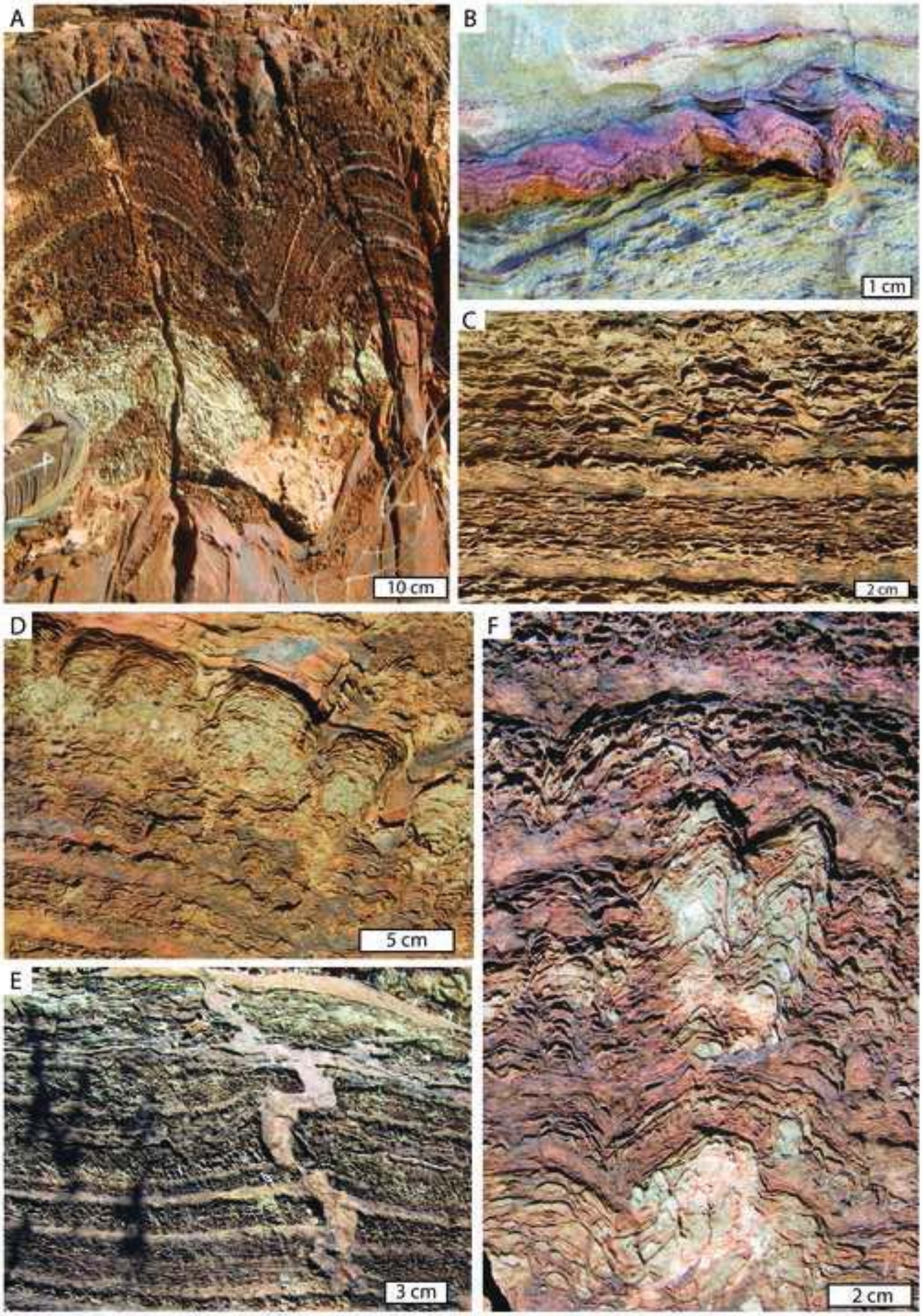

Figure 11

Click here to download high resolution image

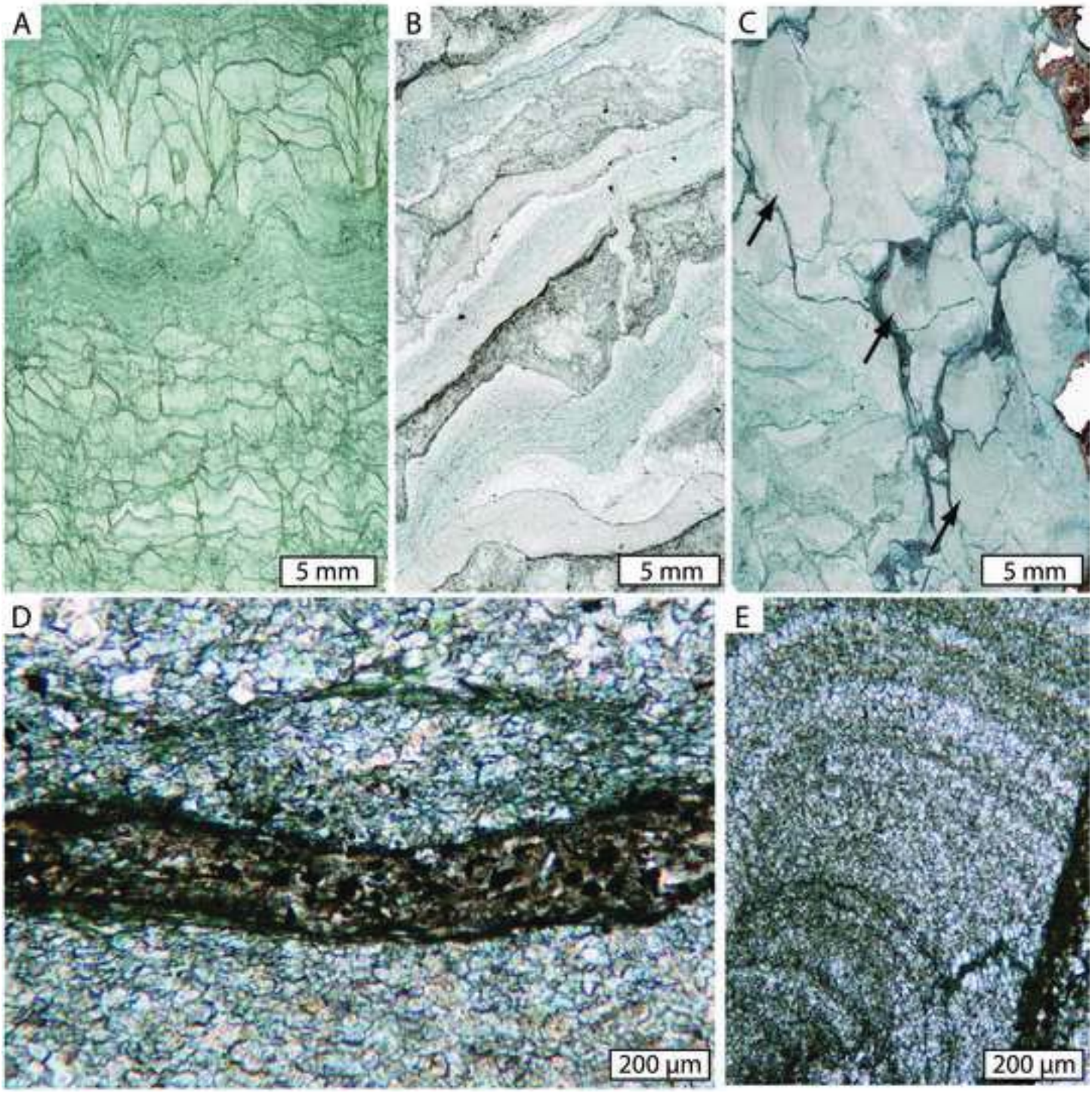

Figure 12

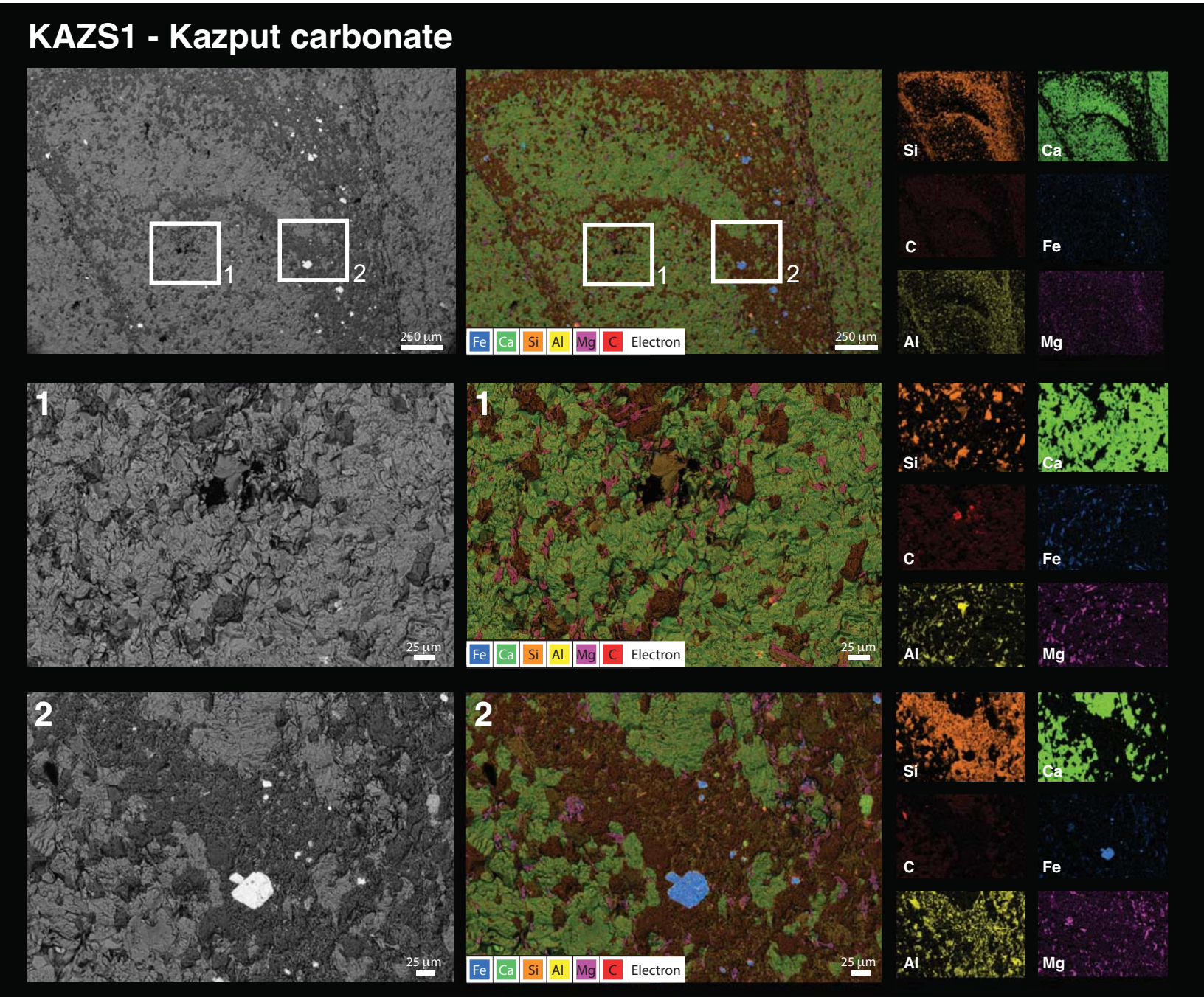
KAZS1 - Kazput carbonate
1
2
250 µm
Fe
Ca
Si
Al
Mg
C
Electron
Si
Ca
C
Fe
Al
Mg
25 µm